

# An Inversion of $\text{NO}_x$ and NMVOC Emissions using Satellite Observations during the KORUS-AQ Campaign and Implications for Surface Ozone over East Asia

5 Amir H. Souri<sup>1\*</sup>, Caroline R. Nowlan<sup>1</sup>, Gonzalo González Abad<sup>1</sup>, Lei Zhu<sup>1,2</sup>, Donald R. Blake<sup>3</sup>, Alan Fried<sup>4</sup>, Andrew J. Weinheimer<sup>5</sup>, Jung-Hun Woo<sup>6</sup>, Qiang Zhang<sup>7</sup>, Christopher E. Chan Miller<sup>1</sup>, Xiong Liu<sup>1</sup>, and Kelly Chance<sup>1</sup>

10 <sup>1</sup>Harvard-Smithsonian Center for Astrophysics, Cambridge, MA, USA  
<sup>2</sup>School of Environmental Science and Engineering, Southern University of Science and Technology, Shenzhen, China  
<sup>3</sup>Department of Chemistry, University of California, Irvine, Irvine, CA, USA  
<sup>4</sup>Institute of Arctic & Alpine Research, University of Colorado, Boulder, CO, USA  
15 <sup>5</sup>National Center for Atmospheric Research, Boulder, CO, USA  
<sup>6</sup>Department of Advanced Technology Fusion, Konkuk University, Seoul, South Korea  
<sup>7</sup>Department of Earth System Science, Tsinghua University, Beijing, China

\* corresponding author: ahsouri@cfa.harvard.edu

20 **Abstract.** The absence of up-to-date emissions has been a major impediment to accurately simulate aspects of atmospheric chemistry, and to precisely quantify the impact of changes in emissions on air pollution. Hence, a non-linear joint analytical inversion (Gauss-Newton method) of both volatile organic compounds (VOC) and nitrogen oxides ( $\text{NO}_x$ ) emissions is made by  
25 exploiting the Smithsonian Astrophysical Observatory (SAO) Ozone Mapping and Profiler Suite Nadir Mapper (OMPS-NM) formaldehyde (HCHO) and the National Aeronautics and Space Administration (NASA) Ozone Monitoring Instrument (OMI) tropospheric nitrogen dioxide ( $\text{NO}_2$ ) retrievals during the Korea-United States Air Quality (KORUS-AQ) campaign over East Asia in May-June 2016. Effects of the chemical feedback of  $\text{NO}_x$  and VOCs on both  $\text{NO}_2$  and  
30 HCHO are implicitly included through iteratively optimizing the inversion. Emission uncertainties are greatly narrowed (averaging kernels  $> 0.8$ , which is the mathematical presentation of the partition of information gained from the satellite observations with respect to the prior knowledge) over medium- to high-emitting areas such as cities and dense vegetation. The prior amount of total  $\text{NO}_x$  emissions is mainly dictated by values reported in the MIX-Asia 2010 inventory. After the  
35 inversion we conclude a decline in the emissions (before, after, change) for China ( $87.94 \pm 44.09$  Gg/day,  $68.00 \pm 15.94$  Gg/day, -23%), North China Plain (NCP) ( $27.96 \pm 13.49$  Gg/day,  $19.05 \pm 2.50$

Gg/day, -32%), Pearl River Delta (PRD) ( $4.23 \pm 1.78$  Gg/day,  $2.70 \pm 0.32$  Gg/day, -36%), Yangtze River Delta (YRD) ( $9.84 \pm 4.68$  Gg/day,  $5.77 \pm 0.51$  Gg/day, -41%), Taiwan ( $1.26 \pm 0.57$  Gg/day,  $0.97 \pm 0.33$  Gg/day, -23%), and Malaysia ( $2.89 \pm 2.77$  Gg/day,  $2.25 \pm 1.34$  Gg/day, -22%), all of which have effectively implemented various stringent regulations. In contrast, South Korea ( $2.71 \pm 1.34$  Gg/day,  $2.95 \pm 0.58$  Gg/day, +9%) and Japan ( $3.53 \pm 1.71$  Gg/day,  $3.96 \pm 1.04$  Gg/day, +12%) experience an increase in  $\text{NO}_x$  emissions potentially due to risen number of diesel vehicles and new thermal power plants. We revisit the well-documented positive bias (by a factor of 2 to 3) of the MEGAN v2.1 in terms of biogenic VOC emissions in the tropics. The inversion, however, suggests a larger growth of VOC (mainly anthropogenic) over NCP (25%) than previously reported (6%) relative to 2010. The spatial variation in both magnitude and sign of  $\text{NO}_x$  and VOC emissions results in non-linear responses of ozone production/loss. Due to simultaneous decrease/increase of  $\text{NO}_x$ /VOC over NCP and YRD, we observe a ~53% reduction in the ratio of the chemical loss of  $\text{NO}_x$  ( $\text{LNO}_x$ ) to the chemical loss of  $\text{RO}_x$  ( $\text{RO}_2 + \text{HO}_2$ ) transitioning toward  $\text{NO}_x$ -sensitive regimes, which in turn, reduces/increases the afternoon chemical loss/production of ozone through  $\text{NO}_2 + \text{OH}$  ( $-0.42$  ppbv  $\text{hr}^{-1}$ )/ $\text{HO}_2$  (and  $\text{RO}_2$ )+ $\text{NO}$  ( $+0.31$  ppbv  $\text{hr}^{-1}$ ). Conversely, a combined decrease in  $\text{NO}_x$  and VOC emissions in Taiwan, Malaysia, and southern China suppresses the formation of ozone. Simulations using the updated emissions indicate increases in maximum daily 8-hour average (MDA8) surface ozone over China (0.62 ppbv), NCP (4.56 ppbv), and YRD (5.25 ppbv), suggesting that emission control strategies on VOCs should be prioritized to curb ozone production rates in these regions. Taiwan, Malaysia, and PRD stand out as the regions undergoing lower MDA8 ozone levels resulting from the  $\text{NO}_x$  reductions occurring predominantly in  $\text{NO}_x$ -sensitive regimes.

## 60 Introduction

The study of ozone ( $O_3$ ) formation within the troposphere in East Asia is of global importance. This significant pollutant is not confined to the source, as it spreads hemispherically through the air, affecting background concentrations as far away as the U.S. A study by Lin et al. [2017] provided modeling evidence of enhancements of springtime surface ozone levels (+0.5 ppbv yr<sup>-1</sup>) in the western U.S. in 1980-2014 solely due to the tripling of Asian anthropogenic emissions over the period. As more studies have informed the impact of ozone pollution on both human health and crop yields, Chinese governmental regulatory agencies have begun to take action on cutting the amount of  $NO_x$  ( $NO+NO_2$ ) emissions since 2011-2012 [Gu et al., 2013; Reuter et al., 2014; Krotkov et al., 2016; de Foy et al., 2016; Souri et al., 2017a]; however no effective policy on volatile organic compound (VOC) emissions had been put into effect prior to 2016 [Stavrakou et al., 2017; Souri et al., 2017a; Shen et al., 2019; Li et al., 2019], with an exception to Pearl River Delta (PRD) [Zhong et al. 2013]. In addition to China, a number of governments including those of Malaysia and Taiwan have put a great deal of effort into shifting their energy pattern from consuming fossil fuels to renewable sources [Trappey et al., 2012; Chua and Oh, 2011]. On the other hand, using satellite observations, Irie et al. [2016] and Souri et al. [2017a] revealed a systematic hiatus in the reduction of  $NO_x$  over South Korea and Japan potentially due to increases in the number of diesel vehicles and new thermal power plants built to compensate for the collapse of the Fukushima nuclear power plant in 2011. Therefore, it is interesting to quantify to what extent these policies have impacted ozone pollution.

Unraveling the origin of ozone is complicated by a number of factors encompassing the nonlinearity of ozone formation to its sources, primarily from  $NO_x$  and VOCs. Therefore, to be able to quantify the impact of recent emission changes, we have developed a top-down estimate of relevant emission inventories using well-characterized satellite observations. There are a myriad of studies focusing on optimizing the bottom-up anthropogenic and biogenic emissions using satellites observations, which provide high spatial coverage, in conjunction with chemical transport models for VOCs [e.g., Palmer et al., 2003; Shim et al., 2005; Curci et al., 2010; Stavrakou et al., 2009, 2011], and  $NO_x$  [e.g., Martin et al., 2003; Chai et al., 2009; Miyazaki et al., 2017; Souri et al., 2016a, 2017a, 2018]. Most inverse modeling studies do not consider both  $NO_2$  and formaldehyde (HCHO) satellite-based observations to perform a joint-inversion. It has been shown that VOC and  $NO_x$  emissions can affect the production/loss of each other [Marais et al.,

2012; Wolfe et al. 2016; Valin et al., 2016; Sourì et al., 2020]. Consequently, a joint method that incorporates both species while minimizing the uncertainties in their emissions is better suited to address this problem. Dealing with this tangled relationship between VOC-NO<sub>2</sub> and NO<sub>x</sub>-HCHO requires an iteratively non-linear inversion framework to incrementally consider the relationships derived from a chemical transport model. Here we will provide an optimal estimate of NO<sub>x</sub> and VOC emissions during the KORUS-AQ campaign using the Smithsonian Astrophysical Observatory (SAO) Ozone Mapping and Profiler Suite Nadir Mapper (OMPS-NM) HCHO and the National Aeronautics and Space Administration (NASA) Ozone Monitoring Instrument (OMI) NO<sub>2</sub> retrievals whose accuracy and precisions are characterized against rich observations collected during the campaign. Having a top-down constraint on both emissions permits a more precise quantification of the impact of the recent emission changes on different chemical pathways pertaining to ozone formation and loss.

## **Measurements, Modeling and Method**

### ***Remote sensing measurements***

#### ***OMPS HCHO***

OMPS-NM onboard the Suomi National Polar-orbiting Partnership (Suomi NPP) is a UV-backscattered radiation spectrometer launched in October 2011 [Flynn et al., 2014]. Its revisit time is the same as other NASA A-Train satellites, including Aura at approximately 13:30 local time at the equator in ascending mode. OMPS-NM covers 300-380 nm with a resolution of 1 nm full-width half maximum (FWHM). The sensor has a 340×740 pixel charge-coupled device (CCD) array measuring the UV spectra at a spatial resolution of 50×50 km<sup>2</sup> at nadir. The HCHO retrieval has been fully described in González Abad et al. [2015; 2016]. Briefly, OMPS HCHO slant columns are fit using direct radiance fitting [Chance, 1998] in the spectral range 327.7-356.5 nm. The spectral fit requires a reference spectrum as function of the cross-track position as it attempts to determine the number of molecules with respect to a reference (i.e., a differential spectrum fitting). To account for this, we use earthshine radiances over a relatively pristine area in the remote Pacific Ocean within -30° to +30° latitudes. An upgrade to this reference correction is the use of daily HCHO profiles over monthly-mean climatological ones from simulations done by the GEOS-Chem chemical transport model. On average, this leads to a 4% difference in HCHO total columns with respect to using the monthly-mean climatological values (Figure S1). The scattering weights describing the sensitivity of the light path through a simulated atmosphere are calculated using

VLIDORT [Spurr, 2006]. The shape factors used for calculating air mass factors (AMFs) are derived from a regional chemical transport model (discussed later) that is used for carrying out the inversion in the present study. We remove unqualified pixels based on cloud fraction < 40%, solar  
125 zenith angle < 65°, and a main quality flag provided in the data. We oversample the HCHO columns for the period of May-June 2016 using a Cressman spatial interpolator with a 1° radius of influence.

### *OMI Tropospheric NO<sub>2</sub>*

We use NASA OMI tropospheric NO<sub>2</sub> (version 3.1) level 2 data whose retrieval is made  
130 in the violet/blue (402-465 nm) due to strong absorption of the molecule in this wavelength range [Levelt et al., 2018]. The sensor has a nadir spatial resolution of 13×24 km<sup>2</sup> which can extend to 40×160 km<sup>2</sup> at the edge of scanlines. A more comprehensive description of the retrieval and the uncertainty associated with the data can be found in Krotkov et al. [2017] and Choi et al. [2020]. We remove bad pixels based on cloud fraction < 20%, solar zenith angle < 65°, without the row  
135 anomaly, vertical column density (VCD) quality flag = 0, and Terrain Reflectivity < 30%. Similar to the OMPS HCHO, we recalculate AMFs by using shape factors from the chemical transport model used in this study. We oversample the OMI granules using the Cressman interpolator with a 0.25° radius of influence.

### ***Model simulation***

To be able to simulate the atmospheric composition, and to perform analytical inverse  
140 modeling, we set up a 27-km grid resolution regional chemical transport model using the Community Multiscale Air Quality Modeling System (CMAQ) model (v5.2.1, doi:10.5281/zenodo.1212601) [Byun and Schere, 2006] that consists of 328×323 grids covering China, Japan, South Korea, Taiwan and some portions of Russia, India and South Asia (Figure 1).  
145 The time period covered by the simulation is from April to June 2016. We use the month of April for spin-up. The anthropogenic emissions are based on the monthly MIX-Asia 2010 inventory [Li et al., 2015] in the CB05 mechanism. The anthropogenic emissions are mainly grouped into three different sectors, namely mobile, point, and residential (area) sources. We apply a diurnal scale to the mobile sectors used in the National Emission Inventory (NEI)-2011 emission platform to  
150 represent the first-order approximation of traffic patterns. We include biomass burning emissions from the Fire Inventory from NCAR (FINN) v1.6 inventory [Wiedinmyer et al., 2011], and consider the plume rise parametrization used in the GEOS-Chem model (i.e., 60% of emissions

are distributed uniformly in the planetary boundary layer (PBL)). We use the offline Model of Emissions of Gases and Aerosols from Nature (MEGAN) v2.1 model [Guenther et al., 2012] following the high resolution inputs described in Souri et al. [2017]. The diurnally-varying lateral chemical conditions are simulated by GEOS-Chem v10 [Bey et al., 2001] using the full chemistry mechanism (NO<sub>x</sub>-O<sub>x</sub>-HC-Aer-Br) spun up for a year. With regard to weather modeling, we use the Weather Research and Forecasting model (WRF) v3.9.1 [Skamarock et al., 2008] at the same resolution to that of the CMAQ (~27 km), but with a wider grid (342×337), and 28 vertical pressure sigma levels. The lateral boundary conditions and the grid nudging inputs are from the global Final (FNL) 0.25° resolution model. The major configurations for the WRF-CMAQ model are summarized in Table 1 and Table 2.

### *Inverse modeling*

We attempt to improve our high-dimensional imperfect numerical representation of atmospheric compounds using the well-characterized NO<sub>2</sub> and HCHO columns from satellites. We use an analytical inversion using the WRF-CMAQ model to constrain the relevant bottom-up emission estimation [Souri et al., 2016; Souri et al., 2017a; Souri et al., 2018]. The inversion seeks to solve the following cost function under the assumptions that i) both observation and emission error covariances follow Gaussian probability density functions with a zero bias, ii) the observation and emission error covariances are independent and iii) the relationship between observations and emissions is not grossly non-linear:

$$J(\mathbf{x}) = \frac{1}{2}(\mathbf{y} - F(\mathbf{x}))^T \mathbf{S}_o^{-1}(\mathbf{y} - F(\mathbf{x})) + \frac{1}{2}(\mathbf{x} - \mathbf{x}_a)^T \mathbf{S}_e^{-1}(\mathbf{x} - \mathbf{x}_a) \quad (1)$$

where  $\mathbf{x}$  is the inversion estimate (a posteriori) given two sources of data: a priori ( $\mathbf{x}_a$ ) and observation ( $\mathbf{y}$ ).  $\mathbf{S}_o$  and  $\mathbf{S}_e$  are the error covariance matrices of observation (instrument) and emission.  $F$  is the forward model (here WRF-CMAQ) to project the emissions onto columns. The first term of Eq.1 attempts to reduce the distance between observations and the simulated columns. The second term incorporates some prior understanding and expectation of the true state of the emissions. The weight of each term is dictated by its covariance matrix. If  $\mathbf{S}_e$  is large compared to  $\mathbf{S}_o$ , the a posteriori will be independent of the prior knowledge and, conversely, if  $\mathbf{S}_o$  dominates, the final solution will consist mostly of the a priori.

Following the Gauss-Newton method described in Rodger [2000], we derive iteratively (i.e.,  $i$  is the index of iteration) the posterior emissions by:

$$\mathbf{x}_{i+1} = \mathbf{x}_a + \mathbf{G}[\mathbf{y} - F(\mathbf{x}_i) - K_i(\mathbf{x}_i - \mathbf{x}_a)] \quad (2)$$

where  $\mathbf{G}$  is the Kalman gain,

$$\mathbf{G} = \mathbf{S}_e K_i^T (K_i \mathbf{S}_e K_i^T + \mathbf{S}_o)^{-1} \quad (3)$$

and  $K_i (= K(\mathbf{x}_i))$  is the Jacobian matrix calculated explicitly from the model (discussed later). The covariance matrix of the a posteriori is calculated by:

$$\hat{\mathbf{S}}_e = (\mathbf{I} - \mathbf{G}\hat{K}^T)\mathbf{S}_e \quad (4)$$

185 where  $\hat{K}$  is the Jacobian from the *i*th iteration. Here we iterate Eq.2 three times. The averaging kernels ( $\mathbf{A}$ ) are given by:

$$\mathbf{A} = \mathbf{I} - \hat{\mathbf{S}}_e \mathbf{S}_e^{-1} \quad (5)$$

The inversion system is complicated by the commonly overlooked fact that observations are biased. For instance, Souri et al. [2018] found that airborne remote sensing observations were high relative to surface Pandora measurements. The overestimation of the VCDs was problematic, since it could have been propagated in the inversion, inducing a bias in the top-down estimation. The authors partly mitigated it by constraining the MODIS albedo which was assumed to be responsible for the bias. Attempts to reduce the bias resulting from coarse profiles from a global model in calculating gas shape profiles were made by recalculating the shape factors using those from higher spatial resolution regional models in other studies [e.g., Souri et al., 2017; Laughner et al., 2018]. For this study, we use abundant observations from the KORUS-AQ campaign and follow the intercomparison platform proposed by Zhu et al. [2016; 2020] using aircraft observations to be able to mitigate the biases in HCHO columns. Based on the corrected global model as a benchmark (Figure S2), we scale up all OMPS HCHO columns by 20%. To mitigate the potential biases in OMI NO<sub>2</sub>, we followed exclusively the values reported over the KORUS-AQ period in Choi et al. [2020]. We increase the NO<sub>2</sub> concentration uniformly by 33.9% (see table A3 in the paper).

205 We calculate the covariance matrix of observations using the column uncertainty variable provided in the satellite datasets and consider them as random errors associated with spectrum fitting. We consider 25% random errors for the air mass factors. Therefore, these values (as random errors) are significantly lowered down by oversampling the data over the course of two months. In addition to that, we consider a fixed error for all pixels due to variability that exists in the applied bias correction ( $3.61 \times 10^{15}$  molec.cm<sup>-2</sup> for NO<sub>2</sub> and  $4.62 \times 10^{15}$  molec.cm<sup>-2</sup> for HCHO). This error

is based on the RMSE obtained from the mentioned studies used for removing biases. Despite the fact that we do not account for non-diagonal elements of the covariance matrices, the incremental updates of  $\mathbf{G}$  adjusted by both  $\text{NO}_2$  and  $\text{HCHO}$  observations should better translate the covariance matrices into the emission space.

To increase the degree of freedom for the optimization, we combine all sector emissions including anthropogenic, biomass burning and biogenic emissions for  $\text{NO}_x$  and VOCs. Therefore, we use the following formula to estimate the variance of the a priori:

$$\sigma_{Total}^2 = f_{Anthro}^2 \times \sigma_{Anthro}^2 + f_{BB}^2 \times \sigma_{BB}^2 + f_{Bio}^2 \times \sigma_{Bio}^2 \quad (6)$$

where  $f$  denotes the fraction of the emission sector with respect to the total emissions, and  $\sigma$  is the standard deviation of each sector category which is calculated from the average of each sector to a relative error listed in Table 3.

For the same purpose (enhancing the amount of information gained from satellite observation) and to increase computational speed, we reduce the dimension of the state vectors (emissions) by aggregating them. However, grouping emissions into certain zones could also introduce another type of uncertainty, known as the aggregation error. We choose optimally aggregated zones by running the inversion multiple times, each with a certain selection of state vectors [Turner and Jacob, 2015]. As in our previous study in Souri et al. [2018], we use the Gaussian Model Mixture (GMM) method to cluster emissions into certain zones that share roughly similar features and investigate which combinations will lead to a minimum of the sum of aggregation and smoothing errors.

In order to create the  $K$  matrix, one must estimate the impact of changes in emissions for each of the aggregated zones to the concentrations of a target compound which is calculated using CMAQ-Direct Decoupled Method (DDM) [Dunker et al., 1989; Cohan et al., 2005]. For instance, the first row and column of  $K$  denoting the response of the first grid cell to a zonal emission can be obtained by:

$$K_{(1,1)} = \frac{S_{(1,1)}^{NO_2}}{ENO_x^{Total,Zone}} \quad (7)$$

where  $S_{(1,1)}^{NO_2}$  is the DDM output in units of molecule  $\text{cm}^{-2}$  for the first row and column. It explains the resultant change in  $\text{NO}_2$  column by changing one unit of total  $\text{NO}_x$  emissions. The same concept will be applied to  $\text{HCHO}$  and VOC emissions. We do not consider the transport between zones due to computational burdens; therefore, we assume that the  $\text{HCHO}$  and  $\text{NO}_2$  columns are



mostly confined to their sources in the two-month averages. The advantage of using CMAQ-DDM to estimate the sensitivity lies in the fact that it calculates the local gradient which better represents the non-linear relationship existing between the emissions and the columns [Souri et al., 2017a; Souri et al., 2018], which in turn, it reduces the number of iterations.

#### 240 **Validation of the model in terms of meteorology**

It is essential to first evaluate some key meteorological variables, because large errors in the weather can complicate the inversion [e.g., Liu et al. 2017]. In order to validate the performance of the WRF model in terms of a number of meteorological variables including surface temperature, relative humidity, and winds, we use more than 1100 surface measurements from integrated  
245 surface database (ISD) stations (<https://www.ncdc.noaa.gov/isd>) over the domain in May-June 2016. Table 4 lists the comparison of the model and the observations for the mentioned variables. Our model demonstrates a very low bias (0.6°C) with regard to surface temperature. We find a reasonable correspondence in terms of relative humidity indicating a fair water vapor budget in the model. The largest discrepancy between the model and observations with respect to  
250 temperature and humidity occurs in those grid cells that are in the proximity of the boundary conditions (not shown). Concerning the wind components, the deviation of the model from the observations is smaller than results obtained in a relatively flat area like Houston in Souri et al. [2016].

#### **Comparison to satellites and providing top-down emissions**

255 Prior to updating the emissions, we find it necessary to shed light on the spatial distribution of tropospheric NO<sub>2</sub> and HCHO columns from both observations and model, and their potential differences relative to their key precursors' emissions. Subsequently, we report the results from the inverse modeling and the uncertainty associated with the top-down estimation; moreover, we wish to assess how much information is gained from utilizing satellite observations via the  
260 calculation of averaging kernels. Finally, observations are used to verify, to some extent, the accuracy of our top-down emission estimations.

#### **NO<sub>x</sub>**

The first row in Figure 2 illustrates tropospheric NO<sub>2</sub> columns from the regional model, OMI (using adjusted AMF and bias corrected), and the natural logarithmic ratio of both quantities  
265 in May-June 2016 at ~1330 LST over Asia. The second row depicts daily-mean values of dominant sources of NO<sub>x</sub>, namely as, biogenic, anthropogenic, and biomass burning emissions (that are

subject to change after the inversion). A high degree of correlation between the anthropogenic NO<sub>x</sub> emissions and NO<sub>2</sub> columns implies the predominant production of NO<sub>2</sub> from the anthropogenic sources [Logan, 1983]. We find a reasonable two-dimensional Pearson correlation ( $r=0.73$ )  
270 between the modeled and the observed columns. Generally, the WRF-CMAQ largely underestimated (56%,  $-7.72 \times 10^{14}$  molec.cm<sup>-2</sup>) tropospheric NO<sub>2</sub> columns with respect to those of OMI over the entire domain. Segregating intuitively the domain into high emission areas (NO<sub>x</sub> > 10 ton/day) and low ones (NO<sub>x</sub> < 10 ton/day) allows for a better understanding of the discrepancy between the model and the observations. In the high NO<sub>x</sub> areas, the model tends to overestimate  
275 tropospheric NO<sub>2</sub> columns by 73% ( $3.71 \times 10^{15}$  molec.cm<sup>-2</sup>), whereas for the low NO<sub>x</sub> regions, the model shows a substantial underestimation by 68% ( $-8.97 \times 10^{14}$  molec.cm<sup>-2</sup>). Such a conflicting bias is confirmed by the contour map of the logarithm ratio of OMI to the model in Figure 2. The large overestimation of the model in terms of NO<sub>2</sub> over the polluted areas is explained by stringent regulations enacted in various countries in Asia; for instance, Chinese regulatory agencies have  
280 taken aggressive actions recently to cut anthropogenic NO<sub>x</sub> emissions by implementing selective catalytic reduction in power plants, closing a number of coal power plants, and policies on transportation [Zhang et al., 2012; Liu et al., 2016; Reuter et al., 2015; de Foy et al., 2016; Krotkov et al., 2016; Souri et al., 2017a]. The highest positive bias in the model is observed over Shanxi Province in China, home to coal production, underscoring the effectiveness of the emission  
285 standards at controlling NO<sub>x</sub> emissions. Likewise, we observe a positive bias in the model over major cities in Japan and South Korea; but the magnitude of the reduction over these cities is substantially smaller than what we observe in China.

The underestimation of the model in the low NO<sub>x</sub> regions is related to a number of factors such as i) the widely-reported underestimation of soil (biogenic) NO<sub>x</sub> emissions due to the lack of  
290 precise knowledge of fertilizers use, soil biota, or canopy interactions [Jaeglé, et al., 2005; Hudman et al., 2010; Souri et al., 2016a], ii) the underestimation of the upper-troposphere NO<sub>2</sub> due to non-surface emissions (aviation/lightning) or errors in the vertical mixing or moist convection [e.g., Souri et al., 2018], and iii) a possible overprediction of the lifetime of organic nitrates diminishing  
295 background NO<sub>2</sub> levels [Canty et al., 2015]. Addressing the second issue requires a very high resolution model with explicit resolving microphysics and large eddy simulations, and the last problem requires more experimental studies to improve organic nitrates chemistry [Romer Present et al., 2020]. In this study, we attempt to mitigate the discrepancy between the model and the

satellite observations solely by adjusting the relevant emissions. Accordingly, future improvements in physical/chemical processes of models will offset top-down emission estimates, inevitably.

The first row in Figure 3 shows the a priori, the a posteriori, and their ratios in terms of the total NO<sub>x</sub> emissions in May-June 2016. We observe that the ratios are highly anti-correlated with those of OMI/CMAQ shown in Figure 2, suggesting that the inversion attempts to reduce the distance between the model and the observations. Major reductions occur over China. The enhancements in NO<sub>x</sub> emissions are commonly found in rural areas, especially over grasslands located in the western/central China and Mongolia. The changes in NO<sub>x</sub> emissions over South Korea and Japan are positive [Irie et al., 2016; Souri et al., 2017a] mainly due to rapid increases in the number of diesel cars in South Korea, and thermal power plants built as a substitution for the Fukushima nuclear plant in Japan. This is especially the case for Japan for which we observe a larger enhancement in total NO<sub>x</sub> emissions (12%). The second row in Figure 3 depicts the relative errors in the a priori, the a posteriori, and AKs. Relative errors in the a priori are mostly confined to values close to 50% in polluted areas. They increase further, up to 100%, in areas experiencing relatively large contributions from biomass burning or biogenic (soil) emissions. Encouragingly, OMI tropospheric NO<sub>2</sub> columns in conjunction with the solid mathematical inversion method [Rodger, 2000] greatly reduce the uncertainties associated with the emissions in polluted areas; we observe AKs close to 1 over major cities or industrial areas. We see the lowest values in AKs over rural areas due to weaker signal/noise ratios from the sensor. Therefore, it is desirable but very difficult to improve the model using the sensor with respect to NO<sub>x</sub> chemistry/emissions in remote areas, evident in the low values of AKs. Table 5 lists the magnitude of the total NO<sub>x</sub> emissions in several regions (refer to Figure 1) before and after carrying out the inversion. If we assume that the dominant source of NO<sub>x</sub> emissions is anthropogenic, the most successful countries at cutting emissions (before, after) are China (87.94±44.09 Gg/day, 68.00±15.94 Gg/day), Taiwan (1.26±0.57 Gg/day, 0.97±0.33 Gg/day), and Malaysia (2.89±2.77 Gg/day, 2.25±1.34 Gg/day). All three countries have successfully implemented regulations to reduce anthropogenic emissions since 2010-2011 [Zhang et al., 2012; Trappey et al., 2012; Chua and Oh, 2011]. The uncertainty associated with the top-down estimate improves considerably. The largest reduction in the uncertainty of the emissions is observed over China, a response to a strong signal from OMI.

An interesting observation lies in the discrepancy between the logarithm-ratio of OMI/CMAQ (Figure 2) to that of the a posteriori to the a priori over the North China Plain (NCP), suggesting that using a bulk ratio [Martin et al., 2003] cannot fully account for possible chemical feedback. The logarithm-ratio of OMI/CMAQ is consistently lower than the changes in the emission. Two reasons contribute to this effect: i) as  $\text{NO}_x$  emissions decrease in  $\text{NO}_x$ -saturated areas (i.e., the dominant sink of radicals is through  $\text{NO}_2 + \text{OH}$ ), OH levels essentially increase resulting in a shorter lifetime in  $\text{NO}_2$ ; therefore to reduce  $\text{NO}_2$  concentrations, a substantial reduction in  $\text{NO}_x$  (suggested by OMI/CMAQ) is unnecessary coinciding with results from the inverse modeling, ii) the CMAQ-DDM (Figure S3) suggests that  $\text{NO}_2$  columns decrease due to increasing VOC emissions over the region; accordingly, the cross-relationship between  $\text{NO}_2$  concentrations and VOC emissions partly adds to the discrepancy. It is because of the chemical feedback that recent studies have attempted to enhance the capability of inverse modeling by iteratively adjusting relevant emissions [e.g., Cooper et al., 2017; Li et al., 2019]. Likewise, our iterative non-linear inversion shows a superior performance over traditional bulk ratio methods, in part because it considered incrementally the chemical feedback.

To assess the resulting changes in the tropospheric  $\text{NO}_2$  columns after the inversion, and to validate our results, we compare the simulated values using the a priori and the a posteriori with OMI in Figure 4. We observe 64% reduction in the tropospheric  $\text{NO}_2$  columns on average over NCP despite only 32% reduction in the total  $\text{NO}_x$  emissions over the region, a result of the chemical feedback. The two-dimensional Pearson correlation between the simulation using the a posteriori and OMI increases from 73% (using the a priori) to 83%. Both datasets now are in a better agreement as far as the magnitude goes. However, we do not see a significant change in the background values in the new simulation compared to those of OMI due to less certain column observations.

To further validate the results, we compare the  $\text{NO}_2$  data from the NCAR's four-channel chemiluminescence instrument onboard the DC-8 aircraft during the campaign (Figure S4). These data are not interfered by  $\text{NO}_z$  family. The aircraft collected the data in the Korean Peninsula around 23 days in May-June 2016 covering various altitudes and hours (<https://www-air.larc.nasa.gov/cgi-bin/ArcView/korusaq>, access date: December 2019). We observe an underestimation of  $\text{NO}_2$  at the near surface levels (<900 hPa) by 19% (DC8 = 4.50 ppbv, CMAQ

= 3.67 ppbv). The updated emissions increase the near surface levels over the Korean Peninsula, which in turn, reduce the bias to 11% (CMAQ = 4.02 ppbv).

### 360 *VOC*

A comparison between HCHO columns from the model and OMPS along with the major sources of VOCs in May-June 2016 is depicted in Figure 5. Anthropogenic VOCs are emitted from various sources such as solvent use, mobile, and chemical industries [Liu et al., 2008a,b]. A reasonable correlation ( $r=0.78$ ) between the model and OMPS suggests a good confidence in the location of emissions. However, the magnitude of HCHO columns between the two datasets strongly disagrees, especially over the tropics where biogenic emissions are large. A myriad of studies have reported a largely positive bias (by a factor of 2-3) associated with isoprene emissions estimated by MEGAN using satellite measurements over the tropics [e.g., Millet et al., 2008; Stavrakou et al., 2009; Marais et al., 2012; Bauwens et al., 2016]. To compound, Stavrakou et al. [2011] found a large overestimation in methanol emissions from the same model that can further preclude the accurate estimation of the yield of HCHO. As a response to the overestimation of the biogenic VOCs by MEGAN, we observe a largely positive bias in the simulated HCHO columns ranging from 50% over the south of China to ~400% over Malaysia and Indonesia. As we move away from the hotspot of the biogenic emissions in lower latitudes, the positive bias of the model declines, ultimately turning into a negative bias at higher latitudes. OMPS HCHO columns suggest that the concentration of HCHO over NCP and Yangtze River Delta (YRD) is comparable to those over the tropics suggesting that the anthropogenic emissions over NCP are the dominant source of HCHO [Souri et al., 2017a; Jin and Holloway, 2015]. We do not see a significant deviation in the model from the observations over this region indicating that no noticeable efforts on controlling VOC emissions in NCP and YRD have been made which is very likely due to the fact that the recent regulations over China have overlooked cutting emissions from several industrial sectors [Liu et al., 2016] prior to 2016 [Li et al. 2019]. For instance, Stavrakou et al. [2017] reported ~6% increases in anthropogenic VOC emissions over China from 2010 to 2014. The underestimation of the model with respect to OMPS lines up with results reported by Souri et al. [2017a] and Shen et al. [2019]. We observe both underestimated and overestimated values in the simulated HCHO columns over areas in South Korea and Japan. The underestimation of HCHO in the model over regions with low VOCs (such as Mongolia and Pacific Ocean) can be either due to missing sources or the incapability of the WRF-CMAQ to account for moist convective transport.

Figure 6 illustrates the total VOC emissions before and after the inversion along with their errors. Immediately apparent is the large reduction of VOC emissions in the tropics and subtropics due to the overestimation of isoprene from MEGAN v2.1. In contrast, enhancements of the emissions are evident at higher latitudes. We observe that the dominantly anthropogenic VOC emissions over NCP increase (~25%) after the adjustment. Despite the presence of vegetation over Japan and South Korea, we do not see the emissions are severely overestimated. Hence, the overestimation of isoprene emissions is more pronounced in the tropics possibly because of an overestimation in the emission factors used for specific plants. Nevertheless, a non-trivial oversight in models could be an insufficient representation of both HO<sub>x</sub> chemistry and dry deposition in forest canopies [Millet et al., 2008]; as a result, the net amount of HCHO in the atmosphere over forest areas is higher than what should be if removal through either a chemical loss or a faster dry deposition was considered.

Owing to the fact that we assume anthropogenic VOC emissions to be less uncertain relative to other sectors, the errors in the a priori are smaller in populated areas. We observe that OMPS HCHO columns are able to significantly reduce the uncertainty associated with the total VOC emissions over areas showing a strong HCHO signal ( $>10^{16}$  molec.cm<sup>-2</sup>). Over clean areas, it is the other way around; we see less confidence in our top-down estimate (AK<0.4) in areas such as Tibet and Mongolia.

We then compare the simulated HCHO column using two different emission inventories with those of OMPS in Figure 7. We observe a substantial improvement both in the spatial structure and the magnitude of simulated HCHO columns using the a posteriori with respect to OMPS. The two-dimensional Pearson correlation increases from 0.78 to 0.91 after applying the adjustments to the emissions. In response to the increases in the total VOC emissions over the NCP, we observe ~11% enhancements in the simulated HCHO total columns. The updated emissions lead to a reduction in HCHO total columns as large as 70% in the tropics.

Validation of the model in terms of VOCs is not a straightforward task because the chemical mechanism used for our model has lumped several VOC species such as terminal/internal olefin or paraffin, only a handful of which were measured during the campaign. Besides, the MIX-Asia inventory estimates the anthropogenic emissions for a selected number of VOCs in the CB05 mechanism. Here, we focus only on six compounds including isoprene, HCHO, ethene, ethane, acetaldehyde, and methanol whose emissions are adjusted (with the same factor) based on satellite

420 measurements. The comparison of the simulated values with the DC-8 measurements showed a noticeable mitigation in the discrepancy between two datasets at lower boundaries (<900 hPa) in terms of isoprene (Figure S5), ethane (Figure S6), ethene (Figure S7), and acetaldehyde (Figure S8). Surprisingly, we observe a large underestimation of methanol over the Korean Peninsula by a factor of ten (Figure S9). The same tendency was observed in other regions in Wells et al. [2014] (see Figure 8 in the paper). Our inversion obviously fails at mitigating the bias as there is not much direct constraints from the satellite observations on this compound. Wells et al. [2014] and Hu et al. [2011] demonstrated that methanol can be a secondary source of HCHO up to 10-20% in midlatitudes in warm seasons. We tend to underestimate HCHO concentrations (by 15%) in the lower atmosphere (<900 hPa) after using the a posteriori over the Korean Peninsula (Figure S10).

### 430 **Implications for surface ozone**

The results we have generated can be further exploited to elucidate changes in the ozone production rates  $P(O_3)$  due to having the constrained  $NO_x$  and VOC emissions. We calculate  $P(O_3)$  by subtracting the ozone loss driven by  $HO_x$  ( $HO+HO_2$ ), reaction with several VOCs (i.e., alkenes and isoprene), the formation of  $HNO_3$ , and  $O_3$  photolysis followed by the reaction of  $O(^1D)$  with water vapor, from the ozone formation via removal of  $NO$  through  $HO_2$  or  $RO_2$ :

$$\begin{aligned}
 P(O_3) = & k_{HO_2+NO}[HO_2][NO] + \sum k_{RO_{2i}+NO}[RO_{2i}][NO] \\
 & - k_{OH+NO_2+M}[OH][NO_2][M] - k_{HO_2+O_3}[HO_2][O_3] \\
 & - k_{OH+O_3}[OH][O_3] - k_{O(^1D)+H_2O}[O(^1D)][H_2O] - L(O_3 + VOCs)
 \end{aligned} \tag{8}$$

Since  $P(O_3)$  is a non-linear function of  $NO_x$  and VOC emissions, it is advantageous to look at the ratio of chemical loss of  $NO_x$  to that of  $RO_x$  ( $RO_2+HO_2$ ), a robust indicator to pinpointing underlying drivers for  $RO_x$  cycle.  $LRO_x$  is defined through the sum of primarily radical-radical reactions:

$$LRO_x = k_{HO_2+HO_2}[HO_2]^2 + \sum k_{RO_{2i}+HO_2}[RO_{2i}][HO_2] + \sum k_{RO_{2i}+RO_{2i}}[RO_{2i}]^2 \tag{9}$$

440  $LNO_x$  mainly occurs via the  $NO_2+OH$  reaction:

$$LNO_x = k_{OH+NO_2+M}[OH][NO_2][M] \tag{10}$$

Typically, a value of  $LNO_x/LRO_x \sim 2.7$  defines the transition line between VOC-sensitive and  $NO_x$ -sensitive regimes [Schroeder et al., 2017; Souri et al., 2020].

Figure 8 depicts a contour map of  $LNO_x/RO_x$  ratios before and after the inversion. As expected, the larger ratios are confined within major cities or industrial areas due to abundant  $NO_x$

445 emissions. The hotspot of VOC-sensitive regimes is located in NCP and YRD. Also of interest in  
Figure 8 is that advection renders a major fraction of the Yellow Sea (the sea connecting China to  
Korea) VOC-sensitive. Using the a posteriori leads to precipitous changes in the chemical regimes.  
As a result of a large reduction in the isoprene emissions in both the tropics and subtropics, we  
observe a shift toward VOC-limited, though the values of  $LNO_x/RO_x$  are yet too far from the  
450 transition line (i.e.,  $\ll 2.7$ ). The substantial reduction in  $NO_x$  emissions and an increase in VOC  
emissions over NCP and YRD go hand-in-hand transitioning towards  $NO_x$ -sensitive regime. The  
ratios over South Korea and Japan are found to be variable and somehow in synch with the changes  
in  $NO_x$  emissions.

The resultant changes in the  $LNO_x/LRO_x$  ratios shed some light on ozone sensitivity with  
455 respect to its major precursors, but  $P(O_3)$  is also dependent on the absolute values of emissions,  
the degree of reactivity of VOCs, and the abundance of radicals. Here we use the integrated  
reaction rates (IRR) to determine the most influential reactions pertaining to ozone loss and  
production at the surface. We focus on 1200 to 1800 China standard time (CST) hours. Figure 9  
shows the differences in the major pathways for the loss and the formation of ozone at the surface  
460 within the time window. The differences are computed based on the subtraction of the simulation  
with the a posteriori from that with the a priori. In Figure 9 we see a strong degree of correlation  
between the changes in magnitude of  $P(O_3)$  through  $HO_2+NO$  reaction with those of  $NO_x$   
emissions (Figure 3), whereas the changes in magnitude of  $P(O_3)$  via  $RO_2+NO$  reaction primarily  
are on par with those of VOC emissions (Figure 6). We observe  $P(O_3)$  increases through  $HO_2+NO$   
465 and  $RO_2+NO$  reactions in Japan, South Korea, Myanmar, and Philippines because of increases in  
 $NO_x$  emissions in  $NO_x$ -sensitive regions. The simultaneous decrease in  $NO_x$  and VOC in PRD and  
Taiwan causes the production of ozone via the same pathways to reduce.

Normally, in VOC-rich environments, reduction in VOC emissions boosts OH  
concentrations (Figure S11). Consequently, we observe an enhancement of  $NO_2+OH$  reaction in  
470 the tropics and subtropics. A substantial reduction in the chemical loss of ozone through  $NO_2+OH$   
over NCP and YRD arises from a considerable decrease of  $NO_x$  emissions and an increase in OH  
(due to chemical feedback of  $NO_x$ ). In response to increase in  $HO_x$  concentrations over NCP  
(Figure S11-S12), we observe an enhancement of ozone loss through  $O_3+HO_x$ . The ozone  
photolysis ( $O^1D+H_2O$ ) is majorly driven by photolysis and water vapor mixing ratios, both of  
475 which are roughly constant in both simulations; accordingly the difference map of  $O^1D+H_2O$  is



mainly reflecting changes in ozone concentrations (shown later). Interestingly, we observe a large reduction in the loss of ozone through reaction with VOCs at lower latitudes. This is essentially because of the reduction in ISOP+O<sub>3</sub>, a VOC that prevails in those latitudes. Despite a much slower reaction rate for ISOP+O<sub>3</sub> compared to ISOP+OH and ISOP+hν [Karl et al. 2004], this specific  
480 chemical pathway can be important as a way to oxidize isoprene and form HO<sub>x</sub> in forests [Paulson and Orlando, 1996].

Figure 10 sums the differences of all mentioned chemical pathways involved in formation/loss of surface ozone at 1200-1600 CST. Because of a complex non-linear relationship between P(O<sub>3</sub>) and its precursors, we observe a large variability in both the sign and the amplitude  
485 of P(O<sub>3</sub>). On average, changes in O<sub>3</sub> production dominate over changes in O<sub>3</sub> sinks except in Malaysia which underwent a significant reduction in isoprene emissions, thus slowing down the ISOP+O<sub>3</sub> reaction. In general, the differences in P(O<sub>3</sub>) follow the changes in the NO<sub>x</sub> emissions depending on which chemical regimes prevail.

Much of the above analysis is based on ozone production rates, however, various  
490 parameters encompassing dry deposition, vertical diffusion, and advection can also affect ozone concentrations. Therefore we further compute the difference between the simulated maximum daily 8-h average (MDA8) surface ozone levels before and after the inversion depicted in Figure 11. For comparison, we also overplot the Chinese air quality monitoring network observations (<https://quotsoft.net/air/>) to have a general grasp of the performance of the model before and after  
495 adjusting the emissions. We see a striking correlation between P(O<sub>3</sub>) (right panel in Figure 10) and MDA8 surface ozone indicating that the selected chemical pathways in this study can explain ozone changes. Nonetheless, the transport obviously plays a vital role in the spatial variability associated with the differences of surface ozone [e.g., Souri et al., 2016b]. Figure 11 suggests a significant enhancement of ozone over NCP (~4.56 ppbv, +5.6%) and YRD (5.2 ppbv, +6.8%)  
500 due to simultaneous decreases/increases in NO<sub>x</sub>/VOCs which is in agreement with Li et al. [2019]. On the other hand, reductions in NO<sub>x</sub> mitigate ozone pollution in PRD (-5.4%), Malaysia (-5.6%) and Taiwan (-11.6%). Table 6 lists the simulated MDA8 surface ozone levels for several regions before and after updating the emissions. Increases in MDA8 ozone over NCP and YRD overshadow decreases in southern China resulting in 1.1% enhancement of ozone over China. This  
505 provides strong evidence that regulations on cutting VOC emissions should not be ignored. The largest reduction/increase of MDA8 ozone is found over Taiwan/YRD. Comparisons with surface

observations show that the model generally captured the ozone spatial distributions; however, it tends to largely overpredict MDA8 surface ozone ( $\sim 7$  ppbv). This tendency has been well-documented in other studies [e.g., Travis et al., 2016; Souri et al., 2017b; Lu et al., 2019]. The updated simulation with the top-down emission partly reduces this overestimation in southern regions of China, while it further exacerbates the overestimation in the northern parts. No doubt much of this stems from the fact that the preexisting biases associated with the model (beyond emissions such as vertical mixing and cloud optical thickness) mask any potential improvement expected from the constrained emissions. Because of this, in addition to adjusting relevant emissions, a direct assimilation of ozone concentrations should complementarily be exploited [e.g., Miyazaki et al., 2019] to bolster the capability of the model at simulating ozone.

### Summary

In this paper we have focused on providing a top-down constraint on both volatile organic compound (VOC) and nitrogen oxides ( $\text{NO}_x$ ) emissions using a combination of the error-characterized Smithsonian Astrophysical Observatory (SAO) Ozone Mapping and Profile Suite Nadir Mapper (OMPS-NM) formaldehyde (HCHO) and National Aeronautics and Space Administration (NASA) Ozone Monitoring Instrument (OMI) nitrogen dioxide ( $\text{NO}_2$ ) retrievals during the Korean and United States (KORUS) campaign over East Asia in May-June 2016. Here, we include biogenic, biomass burning and anthropogenic emissions from MEGAN, FINN, and MIX-Asia 2010 inventory, respectively. A key point is that by considering together the satellite observations, we not only implicitly take the chemical feedback existing between HCHO- $\text{NO}_x$  and  $\text{NO}_2$ -VOC into account through iteratively optimizing analytical non-linear inversion, but also to quantify the impact of recent changes in emissions (since 2010) on surface ozone pollution.

Concerning total  $\text{NO}_x$  emissions, the inversion estimate suggests a substantial reduction over China (-23%), North China Plain (NCP) (-32%), Pearl River Delta (PRD) (-36%), Yangtze River Delta (YRD) (-41%), Taiwan (-23%), and Malaysia (-22%) with respect to the values reported in the prior emissions mostly dictated by the MIX-Asia 2010 inventory. In essence these values reflect recent actions to lower emissions in those countries [Zhang et al., 2012; Trappey et al., 2012; Chua and Oh, 2011]. The analytical inversion also paves the way for estimating the averaging kernels (AKs), thereby informing the amount of information acquired from satellites on the top-down estimation. We observe  $\text{AKs} > 0.8$  over major polluted areas indicating that OMI is able to improve the emission estimates over medium to high-emitting regions. Conversely, AKs

are found to be small over pristine areas suggesting that little information can be gained from the satellite over rural areas given retrieval errors. In line with the studies of Irie et al. [2016] and Souri et al. [2017a], we observe a growth in the total NO<sub>x</sub> emissions in Japan (12%) and South Korea (+9%) which are partially explained by new construction of thermal power plants in Japan, and an upward trend in the number of diesel vehicles in South Korea.

MEGAN v2.1 estimates too much isoprene emissions in the tropics and subtropics, a picture that emerges from the latitudinal dependence of the posterior VOC emissions to the prior ones. It is readily apparent from the top-down constrained VOC emissions that the prevailing anthropogenic VOC emissions in NCP is underestimated by 25%, a direction that is in agreement with studies by Souri et al. [2017a] and Shen et al. [2019]. We find out that OMPS HCHO columns can greatly reduce the uncertainty associated with the total VOC emissions (AKs>0.8) over regions having a moderate-strong signal (>10<sup>16</sup> molec.cm<sup>-2</sup>).

A large spatial variability associated with both NO<sub>x</sub> and VOC results in great oscillation in chemical conditions regimes (i.e., NO<sub>x</sub>-sensitive or VOC-sensitive). Due to considerable reduction/increase in NO<sub>x</sub>/VOC emissions in NCP and YRD, we observe a large increase (53%) in the ratio of the chemical loss of NO<sub>x</sub> (LNO<sub>x</sub>) to the chemical loss of RO<sub>x</sub> (RO<sub>2</sub>+HO<sub>2</sub>) shifting the regions towards NO<sub>x</sub>-sensitive. As a result, a substantial reduction in afternoon NO<sub>2</sub>+OH reaction rate (a major loss of O<sub>3</sub>), and an increase in afternoon NO+HO<sub>2</sub> and RO<sub>2</sub>+NO (a major production pathway for O<sub>3</sub>) are observed, leading to enhancements of the simulated maximum daily 8-hr average (MDA8) surface ozone concentrations by ~5 ppbv. Therefore, additional regulations on VOC emissions should be implemented to battle ozone pollution in those areas. On the other hand, being predominantly in NO<sub>x</sub>-sensitive regimes favors regions including Taiwan, Malaysia and PRD to benefit from reductions in NO<sub>x</sub>, resulting in noticeable decreases in simulated MDA8 surface ozone levels. The comparison of simulated ozone before and after adjusting emissions and Chinese surface air quality observations reveal a large systematic positive bias (~ 7 ppbv) which hinders attaining the benefits from a more accurate ozone production rate due to the observationally-constrained NO<sub>x</sub>/VOC ratios. This highlights the need to explicitly deal with other underlying issues in the model [e.g., Travis et al., 2016] to be able to properly simulate surface ozone.

It has taken many years to develop satellite-based gas retrievals, and weather and chemical transport models accurate enough to enable observationally-based estimates of emissions with

reasonable confidence and quantified uncertainty, and produce credible top-down emission  
570 inventories over certain areas. However it is essential to improve certain aspects to be able to  
narrow the range of uncertainty associated with the estimation such as i) parameterizing  
spatiotemporally varying bias of the satellite gas retrievals ii) improving the knowledge of prior  
errors in the bottom-up emissions, iii) propagating the model parameter errors such as PBL,  
radiation, and winds to the final output [e.g., Rodger 2000], iv) due to intertwined chemical  
575 feedback between various chemical compounds, inverse modeling needs to properly incorporate  
all available information (beyond HCHO and NO<sub>2</sub>) considering the cross-relationship either  
explicitly or implicitly. Despite these limitations, this research demonstrated that a joint inversion  
of NO<sub>x</sub> and VOC emissions using well-characterized observations significantly improved the  
simulation of HCHO and NO<sub>2</sub> columns, permitting an observationally-constrained quantification  
580 of the response of ozone production rates to the emission changes.

### **Acknowledgment**

We are thankful for the funding from NASA Aura Science Team (#NNX17AH47G), NASA  
Science of Terra, Aqua and Suomi NPP (#80NSSC18K0691), NASA Making Earth System Data  
Records for Use in Research Environments (#80NSSC18M0091), and NOAA AC4 program  
585 (#NA18OAR4310108). We acknowledge the publicly available WRF, CMAQ, GEOS-Chem  
models, and KORUS-AQ data that make this study possible. The simulations were run on the  
Smithsonian Institution High Performance Cluster (SI/HPC) (<https://doi.org/10.25572/SIHPC>).  
Methanol and acetaldehyde measurements aboard the NASA DC-8 during KORUS-AQ were  
supported by the Austrian Federal Ministry for Transport, Innovation and Technology (bmvit)  
590 through the Austrian Space Applications Programme (ASAP) of the Austrian Research Promotion  
Agency (FFG). The PTR-MS instrument team (P. Eichler, L. Kaser, T. Mikoviny, M. Müller, A.  
Wisthaler) is acknowledged for providing the data used in this study.

### **Data Availability**

The top-down emission inventories estimated from this study can be found from:  
595 <http://dx.doi.org/10.17632/8s4jscopy93m.1>

### **Authors' contributions**

A.H.S designed the research, analyzed the data, conducted the inverse modeling, CMAQ, GEOS-  
Chem, WRF, and MEGAN, made all figures and wrote the manuscript. C.R.N, G.G, C.E.C.M,  
X.L. and K.C retrieved OMPS HCHO columns and conceived the study. L.Z. validated OMPS

600 HCHO. D.R.B, A.F, and A.J.W measured different compounds during the campaign. J.W and Q.Z  
provided MIX-Asia inventory. All authors contributed to discussions and edited the manuscript.

**Declaration of Competing Interest**

The authors declare that they have no known competing financial interests or personal  
relationships that could have appeared to influence the work reported in this paper.

605

## References

- 610 Bauwens, M., Stavrakou, T., Müller, J.-F., Smedt, I.D., Roozendaal, M.V., Werf, G.R. van der, Wiedinmyer, C., Kaiser, J.W., Sindelarova, K., Guenther, A., 2016. Nine years of global hydrocarbon emissions based on source inversion of OMI formaldehyde observations. *Atmospheric Chemistry and Physics* 16, 10133–10158. <https://doi.org/10.5194/acp-16-10133-2016>
- 615 Bey, I., Jacob, D.J., Yantosca, R.M., Logan, J.A., Field, B.D., Fiore, A.M., Li, Q., Liu, H.Y., Mickley, L.J., Schultz, M.G., 2001. Global modeling of tropospheric chemistry with assimilated meteorology: Model description and evaluation. *Journal of Geophysical Research: Atmospheres* 106, 23073–23095. <https://doi.org/10.1029/2001JD000807>
- Byun, D., Schere, K.L., 2006. Review of the Governing Equations, Computational Algorithms, and Other Components of the Models-3 Community Multiscale Air Quality (CMAQ) Modeling System. *Appl. Mech. Rev* 59, 51–77. <https://doi.org/10.1115/1.2128636>
- 620 Canty, T.P., Hembeck, L., Vinciguerra, T.P., Anderson, D.C., Goldberg, D.L., Carpenter, S.F., Allen, D.J., Loughner, C.P., Salawitch, R.J., Dickerson, R.R., 2015. Ozone and NOx chemistry in the eastern US: evaluation of CMAQ/CB05 with satellite (OMI) data. *Atmospheric Chemistry and Physics* 15, 10965–10982. <https://doi.org/10.5194/acp-15-10965-2015>
- 625 Chai, T., Carmichael, G.R., Tang, Y., Sandu, A., Heckel, A., Richter, A., Burrows, J.P., 2009. Regional NOx emission inversion through a four-dimensional variational approach using SCIAMACHY tropospheric NO2 column observations. *Atmospheric Environment* 43, 5046–5055. <https://doi.org/10.1016/j.atmosenv.2009.06.052>
- 630 Chance, K., 1998. Analysis of BrO measurements from the Global Ozone Monitoring Experiment. *Geophysical Research Letters* 25, 3335–3338. <https://doi.org/10.1029/98GL52359>
- 635 Choi, S., Lamsal, L.N., Follette-Cook, M., Joiner, J., Krotkov, N.A., Swartz, W.H., Pickering, K.E., Loughner, C.P., Appel, W., Pfister, G., Saide, P.E., Cohen, R.C., Weinheimer, A.J., Herman, J.R., 2020. Assessment of NO2 observations during DISCOVER-AQ and KORUS-AQ field campaigns. *Atmospheric Measurement Techniques* 13, 2523–2546. <https://doi.org/10.5194/amt-13-2523-2020>
- Chua, S.C., Oh, T.H., 2011. Green progress and prospect in Malaysia. *Renewable and Sustainable Energy Reviews* 15, 2850–2861. <https://doi.org/10.1016/j.rser.2011.03.008>
- 640 Cohan, D.S., Hakami, A., Hu, Y., Russell, A.G., 2005. Nonlinear Response of Ozone to Emissions: Source Apportionment and Sensitivity Analysis. *Environ. Sci. Technol.* 39, 6739–6748. <https://doi.org/10.1021/es048664m>
- 645 Cooper, M., Martin, R.V., Padmanabhan, A., Henze, D.K., 2017. Comparing mass balance and adjoint methods for inverse modeling of nitrogen dioxide columns for global nitrogen oxide emissions. *Journal of Geophysical Research: Atmospheres* 122, 4718–4734. <https://doi.org/10.1002/2016JD025985>
- Curci, G., Palmer, P.I., Kurosu, T.P., Chance, K., Visconti, G., 2010. Estimating European volatile organic compound emissions using satellite observations of formaldehyde from the Ozone Monitoring Instrument. *Atmospheric Chemistry and Physics* 10, 11501–11517. <https://doi.org/10.5194/acp-10-11501-2010>

- 650 de Foy, B., Lu, Z., Streets, D.G., 2016. Satellite NO<sub>2</sub> retrievals suggest China has exceeded its  
NO<sub>x</sub> reduction goals from the twelfth Five-Year Plan. *Scientific Reports* 6, 1–9.  
<https://doi.org/10.1038/srep35912>
- Dunker, A.M., 1984. The decoupled direct method for calculating sensitivity coefficients in  
chemical kinetics. *J. Chem. Phys.* 81, 2385–2393. <https://doi.org/10.1063/1.447938>
- 655 Flynn, L., Long, C., Wu, X., Evans, R., Beck, C.T., Petropavlovskikh, I., McConville, G., Yu,  
W., Zhang, Z., Niu, J., Beach, E., Hao, Y., Pan, C., Sen, B., Novicki, M., Zhou, S.,  
Seftor, C., 2014. Performance of the Ozone Mapping and Profiler Suite (OMPS)  
products. *Journal of Geophysical Research: Atmospheres* 119, 6181–6195.  
<https://doi.org/10.1002/2013JD020467>
- 660 González Abad, G., Liu, X., Chance, K., Wang, H., Kurosu, T.P., Suleiman, R., 2015. Updated  
Smithsonian Astrophysical Observatory Ozone Monitoring Instrument (SAO OMI)  
formaldehyde retrieval. *Atmospheric Measurement Techniques* 8, 19–32.  
<https://doi.org/10.5194/amt-8-19-2015>
- González Abad, G., Vasilkov, A., Seftor, C., Liu, X., Chance, K., 2016. Smithsonian  
665 Astrophysical Observatory Ozone Mapping and Profiler Suite (SAO OMPS)  
formaldehyde retrieval. *Atmospheric Measurement Techniques* 9, 2797–2812.  
<https://doi.org/10.5194/amt-9-2797-2016>
- Gu, D., Wang, Y., Smeltzer, C., Liu, Z., 2013. Reduction in NO<sub>x</sub> Emission Trends over China:  
Regional and Seasonal Variations. *Environ. Sci. Technol.* 47, 12912–12919.  
670 <https://doi.org/10.1021/es401727e>
- Guenther, A.B., Jiang, X., Heald, C.L., Sakulyanontvittaya, T., Duhl, T., Emmons, L.K., Wang,  
X., 2012. The Model of Emissions of Gases and Aerosols from Nature version 2.1  
(MEGAN2.1): an extended and updated framework for modeling biogenic emissions.  
*Geoscientific Model Development* 5, 1471–1492. <https://doi.org/10.5194/gmd-5-1471->  
675 [2012](https://doi.org/10.5194/gmd-5-1471-2012)
- Hu, L., Millet, D.B., Mohr, M.J., Wells, K.C., Griffis, T.J., Helmig, D., 2011. Sources and  
seasonality of atmospheric methanol based on tall tower measurements in the US Upper  
Midwest. *Atmospheric Chemistry and Physics* 11, 11145–11156.  
<https://doi.org/10.5194/acp-11-11145-2011>
- 680 Hudman, R.C., Russell, A.R., Valin, L.C., Cohen, R.C., 2010. Interannual variability in soil  
nitric oxide emissions over the United States as viewed from space. *Atmospheric  
Chemistry and Physics* 10, 9943–9952. <https://doi.org/10.5194/acp-10-9943-2010>
- Irie, H., Muto, T., Itahashi, S., Kurokawa, J., Uno, I., 2016a. Turnaround of Tropospheric  
Nitrogen Dioxide Pollution Trends in China, Japan, and South Korea. *Sola* 12, 170–174.  
685 <https://doi.org/10.2151/sola.2016-035>
- Jaeglé, L., Steinberger, L., Martin, R.V., Chance, K., 2005. Global partitioning of NO<sub>x</sub> sources  
using satellite observations: Relative roles of fossil fuel combustion, biomass burning and  
soil emissions. *Faraday Discuss.* 130, 407–423. <https://doi.org/10.1039/B502128F>
- Jin, X., Holloway, T., 2015. Spatial and temporal variability of ozone sensitivity over China  
690 observed from the Ozone Monitoring Instrument. *Journal of Geophysical Research:  
Atmospheres* 120, 7229–7246. <https://doi.org/10.1002/2015JD023250>
- Karl, M., Brauers, T., Dorn, H.-P., Holland, F., Komenda, M., Poppe, D., Rohrer, F., Rupp, L.,  
Schaub, A., Wahner, A., 2004. Kinetic Study of the OH-isoprene and O<sub>3</sub>-isoprene  
reaction in the atmosphere simulation chamber, SAPHIR. *Geophysical Research Letters*  
695 31. <https://doi.org/10.1029/2003GL019189>

- Krotkov, N.A., McLinden, C.A., Li, C., Lamsal, L.N., Celarier, E.A., Marchenko, S.V., Swartz, W.H., Bucsela, E.J., Joiner, J., Duncan, B.N., Boersma, K.F., Veefkind, J.P., Levelt, P.F., Fioletov, V.E., Dickerson, R.R., He, H., Lu, Z., Streets, D.G., 2016. Aura OMI observations of regional SO<sub>2</sub> and NO<sub>2</sub> pollution changes from 2005 to 2015. *Atmospheric Chemistry and Physics* 16, 4605–4629. <https://doi.org/10.5194/acp-16-4605-2016>
- 700
- Laughner, J.L., Zhu, Q., Cohen, R.C., 2018. The Berkeley High Resolution Tropospheric NO<sub>2</sub> product. *Earth System Science Data* 10, 2069–2095. <https://doi.org/10.5194/essd-10-2069-2018>
- 705
- Levelt, P.F., Joiner, J., Tamminen, J., Veefkind, J.P., Bhartia, P.K., Stein Zweers, D.C., Duncan, B.N., Streets, D.G., Eskes, H., A, R. van der, McLinden, C., Fioletov, V., Carn, S., Laatz, J. de, DeLand, M., Marchenko, S., McPeters, R., Ziemke, J., Fu, D., Liu, X., Pickering, K., Apituley, A., González Abad, G., Arola, A., Boersma, F., Chan Miller, C., Chance, K., Graaf, M. de, Hakkarainen, J., Hassinen, S., Ialongo, I., Kleipool, Q., Krotkov, N., Li, C., Lamsal, L., Newman, P., Nowlan, C., Suleiman, R., Tilstra, L.G., Torres, O., Wang, H., Wargan, K., 2018. The Ozone Monitoring Instrument: overview of 14 years in space. *Atmospheric Chemistry and Physics* 18, 5699–5745. <https://doi.org/10.5194/acp-18-5699-2018>
- 710
- Li, C., Martin, R.V., Shephard, M.W., Cady-Pereira, K., Cooper, M.J., Kaiser, J., Lee, C.J., Zhang, L., Henze, D.K., 2019. Assessing the Iterative Finite Difference Mass Balance and 4D-Var Methods to Derive Ammonia Emissions Over North America Using Synthetic Observations. *Journal of Geophysical Research: Atmospheres* 124, 4222–4236. <https://doi.org/10.1029/2018JD030183>
- 715
- Li, K., Jacob, D.J., Liao, H., Shen, L., Zhang, Q., Bates, K.H., 2019. Anthropogenic drivers of 2013–2017 trends in summer surface ozone in China. *PNAS* 116, 422–427. <https://doi.org/10.1073/pnas.1812168116>
- 720
- Li, M., Zhang, Q., Kurokawa, J., Woo, J.-H., He, K., Lu, Z., Ohara, T., Song, Y., Streets, D.G., Carmichael, G.R., Cheng, Y., Hong, C., Huo, H., Jiang, X., Kang, S., Liu, F., Su, H., Zheng, B., 2017a. MIX: a mosaic Asian anthropogenic emission inventory under the international collaboration framework of the MICS-Asia and HTAP. *Atmospheric Chemistry and Physics* 17, 935–963. <https://doi.org/10.5194/acp-17-935-2017>
- 725
- Li, M., Zhang, Q., Zheng, B., Tong, D., Lei, Y., Liu, F., Hong, C., Kang, S., Yan, L., Zhang, Y., Bo, Y., Su, H., Cheng, Y., He, K., 2019. Persistent growth of anthropogenic non-methane volatile organic compound (NMVOC) emissions in China during 1990–2017: drivers, speciation and ozone formation potential. *Atmospheric Chemistry and Physics* 19, 8897–8913. <https://doi.org/10.5194/acp-19-8897-2019>
- 730
- Lin, M., Horowitz, L.W., Payton, R., Fiore, A.M., Tonnesen, G., 2017. US surface ozone trends and extremes from 1980 to 2014: quantifying the roles of rising Asian emissions, domestic controls, wildfires, and climate. *Atmospheric Chemistry and Physics* 17, 2943–2970. <https://doi.org/10.5194/acp-17-2943-2017>
- 735
- Liu, F., Zhang, Q., A, R.J. van der, Zheng, B., Tong, D., Yan, L., Zheng, Y., He, K., 2016. Recent reduction in NO<sub>x</sub> emissions over China: synthesis of satellite observations and emission inventories. *Environ. Res. Lett.* 11, 114002. <https://doi.org/10.1088/1748-9326/11/11/114002>



- 740 Liu, X., Mizzi, A.P., Anderson, J.L., Fung, I.Y., Cohen, R.C., 2017. Assimilation of satellite  
NO<sub>2</sub> observations at high spatial resolution using OSSEs. *Atmospheric Chemistry and  
Physics* 17, 7067–7081. <https://doi.org/10.5194/acp-17-7067-2017>
- Liu, Y., Shao, M., Fu, L., Lu, S., Zeng, L., Tang, D., 2008a. Source profiles of volatile organic  
745 compounds (VOCs) measured in China: Part I. *Atmospheric Environment, PRIDE-PRD  
2004 Campaign : Program of Regional Integrated Experiments on Air Quality over Pearl  
River Delta of China* 42, 6247–6260. <https://doi.org/10.1016/j.atmosenv.2008.01.070>
- Liu, Y., Shao, M., Lu, S., Chang, C.-C., Wang, J.-L., Fu, L., 2008b. Source apportionment of  
ambient volatile organic compounds in the Pearl River Delta, China: Part II. *Atmospheric  
Environment, PRIDE-PRD 2004 Campaign : Program of Regional Integrated  
750 Experiments on Air Quality over Pearl River Delta of China* 42, 6261–6274.  
<https://doi.org/10.1016/j.atmosenv.2008.02.027>
- Lu, X., Zhang, L., Chen, Y., Zhou, M., Zheng, B., Li, K., Liu, Y., Lin, J., Fu, T.-M., Zhang, Q.,  
2019. Exploring 2016–2017 surface ozone pollution over China: source contributions and  
755 meteorological influences. *Atmospheric Chemistry and Physics* 19, 8339–8361.  
<https://doi.org/10.5194/acp-19-8339-2019>
- Logan, J.A., 1983. Nitrogen oxides in the troposphere: Global and regional budgets. *Journal of  
Geophysical Research: Oceans* 88, 10785–10807.  
<https://doi.org/10.1029/JC088iC15p10785>
- Marais, E.A., Jacob, D.J., Kurosu, T.P., Chance, K., Murphy, J.G., Reeves, C., Mills, G.,  
760 Casadio, S., Millet, D.B., Barkley, M.P., Paulot, F., Mao, J., 2012b. Isoprene emissions in  
Africa inferred from OMI observations of formaldehyde columns. *Atmospheric  
Chemistry and Physics* 12, 6219–6235. <https://doi.org/10.5194/acp-12-6219-2012>
- Martin, R.V., Jacob, D.J., Chance, K., Kurosu, T.P., Palmer, P.I., Evans, M.J., 2003. Global  
inventory of nitrogen oxide emissions constrained by space-based observations of NO<sub>2</sub>  
765 columns. *Journal of Geophysical Research: Atmospheres* 108.  
<https://doi.org/10.1029/2003JD003453>
- Millet, D.B., Jacob, D.J., Boersma, K.F., Fu, T.-M., Kurosu, T.P., Chance, K., Heald, C.L.,  
Guenther, A., 2008b. Spatial distribution of isoprene emissions from North America  
derived from formaldehyde column measurements by the OMI satellite sensor. *Journal of  
770 Geophysical Research: Atmospheres* 113. <https://doi.org/10.1029/2007JD008950>
- Miyazaki, K., Eskes, H., Sudo, K., Boersma, K.F., Bowman, K., Kanaya, Y., 2017. Decadal  
changes in global surface NO<sub>x</sub> emissions from multi-constituent satellite data  
assimilation. *Atmospheric Chemistry and Physics* 17, 807–837.  
<https://doi.org/10.5194/acp-17-807-2017>
- 775 Miyazaki, K., Sekiya, T., Fu, D., Bowman, K.W., Kulawik, S.S., Sudo, K., Walker, T., Kanaya,  
Y., Takigawa, M., Ogochi, K., Eskes, H., Boersma, K.F., Thompson, A.M., Gaubert, B.,  
Barre, J., Emmons, L.K., 2019. Balance of Emission and Dynamical Controls on Ozone  
During the Korea-United States Air Quality Campaign From Multiconstituent Satellite  
Data Assimilation. *Journal of Geophysical Research: Atmospheres* 124, 387–413.  
780 <https://doi.org/10.1029/2018JD028912>
- Palmer, P.I., Jacob, D.J., Fiore, A.M., Martin, R.V., Chance, K., Kurosu, T.P., 2003. Mapping  
isoprene emissions over North America using formaldehyde column observations from  
space. *Journal of Geophysical Research: Atmospheres* 108.  
<https://doi.org/10.1029/2002JD002153>

- 785 Paulson, S.E., Orlando, J.J., 1996. The reactions of ozone with alkenes: An important source of HOx in the boundary layer. *Geophysical Research Letters* 23, 3727–3730. <https://doi.org/10.1029/96GL03477>
- Reuter, M., Buchwitz, M., Hilboll, A., Richter, A., Schneising, O., Hilker, M., Heymann, J., Bovensmann, H., Burrows, J.P., 2014. Decreasing emissions of NO<sub>x</sub> relative to CO<sub>2</sub> in East Asia inferred from satellite observations. *Nature Geoscience* 7, 792–795. <https://doi.org/10.1038/ngeo2257>
- 790
- Rodgers, C.D., 2000. *Inverse Methods for Atmospheric Sounding: Theory and Practice*. WORLD SCIENTIFIC. <https://doi.org/10.1142/3171>
- Romer Present, P.S., Zare, A., Cohen, R.C., 2020. The changing role of organic nitrates in the removal and transport of NO<sub>x</sub>. *Atmospheric Chemistry and Physics* 20, 267–279. <https://doi.org/10.5194/acp-20-267-2020>
- 795
- Schroeder, J.R., Crawford, J.H., Fried, A., Walega, J., Weinheimer, A., Wisthaler, A., Müller, M., Mikoviny, T., Chen, G., Shook, M., Blake, D.R., Tonnesen, G.S., 2017. New insights into the column CH<sub>2</sub>O/NO<sub>2</sub> ratio as an indicator of near-surface ozone sensitivity. *Journal of Geophysical Research: Atmospheres* 122, 8885–8907. <https://doi.org/10.1002/2017JD026781>
- 800
- Shen, L., Jacob, D.J., Zhu, L., Zhang, Q., Zheng, B., Sulprizio, M.P., Li, K., Smedt, I.D., Abad, G.G., Cao, H., Fu, T.-M., Liao, H., 2019. The 2005–2016 Trends of Formaldehyde Columns Over China Observed by Satellites: Increasing Anthropogenic Emissions of Volatile Organic Compounds and Decreasing Agricultural Fire Emissions. *Geophysical Research Letters* 46, 4468–4475. <https://doi.org/10.1029/2019GL082172>
- 805
- Shim, C., Wang, Y., Choi, Y., Palmer, P.I., Abbot, D.S., Chance, K., 2005. Constraining global isoprene emissions with Global Ozone Monitoring Experiment (GOME) formaldehyde column measurements. *Journal of Geophysical Research: Atmospheres* 110. <https://doi.org/10.1029/2004JD005629>
- 810
- Skamarock, W.C., Klemp, J.B., 2008. A time-split nonhydrostatic atmospheric model for weather research and forecasting applications. *Journal of Computational Physics, Predicting weather, climate and extreme events* 227, 3465–3485. <https://doi.org/10.1016/j.jcp.2007.01.037>
- 815
- Souri, A.H., Choi, Y., Jeon, W., Li, X., Pan, S., Diao, L., Westenbarger, D.A., 2016a. Constraining NO<sub>x</sub> emissions using satellite NO<sub>2</sub> measurements during 2013 DISCOVER-AQ Texas campaign. *Atmospheric Environment* 131, 371–381. <https://doi.org/10.1016/j.atmosenv.2016.02.020>
- Souri, A.H., Choi, Y., Li, X., Kotsakis, A., Jiang, X., 2016b. A 15-year climatology of wind pattern impacts on surface ozone in Houston, Texas. *Atmospheric Research* 174–175, 124–134. <https://doi.org/10.1016/j.atmosres.2016.02.007>
- 820
- Souri, A.H., Choi, Y., Jeon, W., Woo, J.-H., Zhang, Q., Kurokawa, J., 2017a. Remote sensing evidence of decadal changes in major tropospheric ozone precursors over East Asia. *Journal of Geophysical Research: Atmospheres* 122, 2474–2492. <https://doi.org/10.1002/2016JD025663>
- 825
- Souri, A.H., Choi, Y., Jeon, W., Kochanski, A.K., Diao, L., Mandel, J., Bhave, P.V., Pan, S., 2017b. Quantifying the Impact of Biomass Burning Emissions on Major Inorganic Aerosols and Their Precursors in the U.S. *Journal of Geophysical Research: Atmospheres* 122, 12,020–12,041. <https://doi.org/10.1002/2017JD026788>

- 830 Souri, A.H., Choi, Y., Pan, S., Curci, G., Nowlan, C.R., Janz, S.J., Kowalewski, M.G., Liu, J., Herman, J.R., Weinheimer, A.J., 2018. First Top-Down Estimates of Anthropogenic NO<sub>x</sub> Emissions Using High-Resolution Airborne Remote Sensing Observations. *Journal of Geophysical Research: Atmospheres* 123, 3269–3284. <https://doi.org/10.1002/2017JD028009>
- 835 Souri, A.H., Nowlan, C.R., Wolfe, G.M., Lamsal, L.N., Chan Miller, C.E., Abad, G.G., Janz, S.J., Fried, A., Blake, D.R., Weinheimer, A.J., Diskin, G.S., Liu, X., Chance, K., 2020. Revisiting the effectiveness of HCHO/NO<sub>2</sub> ratios for inferring ozone sensitivity to its precursors using high resolution airborne remote sensing observations in a high ozone episode during the KORUS-AQ campaign. *Atmospheric Environment* 117341. <https://doi.org/10.1016/j.atmosenv.2020.117341>
- 840 Spurr, R.J.D., 2006. VLIDORT: A linearized pseudo-spherical vector discrete ordinate radiative transfer code for forward model and retrieval studies in multilayer multiple scattering media. *Journal of Quantitative Spectroscopy and Radiative Transfer* 102, 316–342. <https://doi.org/10.1016/j.jqsrt.2006.05.005>
- 845 Stavrakou, T., Guenther, A., Razavi, A., Clarisse, L., Clerbaux, C., Coheur, P.-F., Hurtmans, D., Karagulian, F., Mazière, M.D., Vigouroux, C., Amelynck, C., Schoon, N., Laffineur, Q., Heinesch, B., Aubinet, M., Rinsland, C., Müller, J.-F., 2011. First space-based derivation of the global atmospheric methanol emission fluxes. *Atmospheric Chemistry and Physics* 11, 4873–4898. <https://doi.org/10.5194/acp-11-4873-2011>
- 850 Stavrakou, T., Müller, J.-F., Bauwens, M., De Smedt, I., 2017. Sources and Long-Term Trends of Ozone Precursors to Asian Pollution, in: Bouarar, I., Wang, X., Brasseur, G.P. (Eds.), *Air Pollution in Eastern Asia: An Integrated Perspective*, ISSI Scientific Report Series. Springer International Publishing, Cham, pp. 167–189. [https://doi.org/10.1007/978-3-319-59489-7\\_8](https://doi.org/10.1007/978-3-319-59489-7_8)
- 855 Stavrakou, T., Müller, J.-F., Smedt, I.D., Roozendaal, M.V., Werf, G.R. van der, Giglio, L., Guenther, A., 2009. Global emissions of non-methane hydrocarbons deduced from SCIAMACHY formaldehyde columns through 2003–2006. *Atmospheric Chemistry and Physics* 9, 3663–3679. <https://doi.org/10.5194/acp-9-3663-2009>
- 860 Trappey, A.J.C., Trappey, C., Hsiao, C.T., Ou, J.J.R., Li, S.J., Chen, K.W.P., 2012. An evaluation model for low carbon island policy: The case of Taiwan’s green transportation policy. *Energy Policy* 45, 510–515. <https://doi.org/10.1016/j.enpol.2012.02.063>
- 865 Travis, K.R., Jacob, D.J., Fisher, J.A., Kim, P.S., Marais, E.A., Zhu, L., Yu, K., Miller, C.C., Yantosca, R.M., Sulprizio, M.P., Thompson, A.M., Wennberg, P.O., Crouse, J.D., Clair, J.M.S., Cohen, R.C., Laughner, J.L., Dibb, J.E., Hall, S.R., Ullmann, K., Wolfe, G.M., Pollack, I.B., Peischl, J., Neuman, J.A., Zhou, X., 2016. Why do models overestimate surface ozone in the Southeast United States? *Atmospheric Chemistry and Physics* 16, 13561–13577. <https://doi.org/10.5194/acp-16-13561-2016>
- Turner, A.J., Jacob, D.J., 2015. Balancing aggregation and smoothing errors in inverse models. *Atmospheric Chemistry and Physics* 15, 7039–7048. <https://doi.org/10.5194/acp-15-7039-2015>
- 870 Valin, L.C., Fiore, A.M., Chance, K., Abad, G.G., 2016. The role of OH production in interpreting the variability of CH<sub>2</sub>O columns in the southeast U.S. *Journal of Geophysical Research: Atmospheres* 121, 478–493. <https://doi.org/10.1002/2015JD024012>

- 875 Wells, K.C., Millet, D.B., Cady-Pereira, K.E., Shephard, M.W., Henze, D.K., Bousserez, N.,  
Apel, E.C., de Gouw, J., Warneke, C., Singh, H.B., 2014. Quantifying global terrestrial  
methanol emissions using observations from the TES satellite sensor. *Atmospheric  
Chemistry and Physics* 14, 2555–2570. <https://doi.org/10.5194/acp-14-2555-2014>
- 880 Wiedinmyer, C., Akagi, S.K., Yokelson, R.J., Emmons, L.K., Al-Saadi, J.A., Orlando, J.J., Soja,  
A.J., 2011. The Fire INventory from NCAR (FINN): a high resolution global model to  
estimate the emissions from open burning. *Geoscientific Model Development* 4, 625–  
641. <https://doi.org/10.5194/gmd-4-625-2011>
- 885 Wolfe, G.M., Kaiser, J., Hanisco, T.F., Keutsch, F.N., Gouw, J.A. de, Gilman, J.B., Graus, M.,  
Hatch, C.D., Holloway, J., Horowitz, L.W., Lee, B.H., Lerner, B.M., Lopez-Hilifiker, F.,  
Mao, J., Marvin, M.R., Peischl, J., Pollack, I.B., Roberts, J.M., Ryerson, T.B., Thornton,  
J.A., Veres, P.R., Warneke, C., 2016. Formaldehyde production from isoprene oxidation  
across NO<sub>x</sub> regimes. *Atmospheric Chemistry and Physics* 16, 2597–2610.  
<https://doi.org/10.5194/acp-16-2597-2016>
- 890 Zhang, Q., He, K., Huo, H., 2012. Cleaning China’s air. *Nature* 484, 161–162.  
<https://doi.org/10.1038/484161a>
- Zhong, L., Louie, P.K.K., Zheng, J., Yuan, Z., Yue, D., Ho, J.W.K., Lau, A.K.H., 2013.  
Science–policy interplay: Air quality management in the Pearl River Delta region and  
Hong Kong. *Atmospheric Environment, Improving Regional Air Quality over the Pearl  
River Delta and Hong Kong: from Science to Policy* 76, 3–10.  
895 <https://doi.org/10.1016/j.atmosenv.2013.03.012>
- Zhu, L., González Abad, G., Nowlan, C.R., Chan Miller, C., Chance, K., Apel, E.C., DiGangi,  
J.P., Fried, A., Hanisco, T.F., Hornbrook, R.S., Hu, L., Kaiser, J., Keutsch, F.N., Permar,  
W., Clair, J.M.S., Wolfe, G.M., 2020. Validation of satellite formaldehyde (HCHO)  
retrievals using observations from 12 aircraft campaigns. *Atmospheric Chemistry and  
Physics Discussions* 1–25. <https://doi.org/10.5194/acp-2019-1117>
- 900 Zhu, L., Jacob, D.J., Kim, P.S., Fisher, J.A., Yu, K., Travis, K.R., Mickley, L.J., Yantosca, R.M.,  
Sulprizio, M.P., Smedt, I.D., González Abad, G., Chance, K., Li, C., Ferrare, R., Fried,  
A., Hair, J.W., Hanisco, T.F., Richter, D., Jo Scarino, A., Walega, J., Weibring, P.,  
Wolfe, G.M., 2016. Observing atmospheric formaldehyde (HCHO) from space:  
validation and intercomparison of six retrievals from four satellites (OMI, GOME2A,  
905 GOME2B, OMPS) with SEAC4RS aircraft observations over the southeast US.  
*Atmospheric Chemistry and Physics* 16, 13477–13490. <https://doi.org/10.5194/acp-16-13477-2016>

**Table 1.** CMAQ major configurations

CMAQ version	V5.2.1
Chemical Mechanism	CB05 with chlorine chemistry
Lightning NO <sub>x</sub> emission	Included using inline code
Photolysis	Inline including aerosol impacts
Horizontal advection	YAMO (hyamo)
Vertical advection	WRF omega formula (vwrf)
Horizontal mixing/diffusion	Multiscale (multiscale)
Vertical mixing/diffusion	Asymmetric Convective Model version 2 (acm2)
Aerosol	AERO 6 for sea salt and thermodynamics (aero6)
IC/BC source	GEOS-Chem v10

**Table 2.** WRF physics options

WRF Version	V3.9.1
Microphysics	WSM-6
Long-wave Radiation	RRTMG
Short-wave Radiation	RRTMG
Surface Layer Option	Monin-Obukhov
Land-Surface Option	Noah LSM
Boundary Layer	ACM2
Cumulus Cloud Option	Kain-Fritsch
IC/BC	FNL 0.25°

**Table 3.** The uncertainty assumptions used for estimating the covariance matrix of the a priori.

	Anthropogenic	Biogenic	Biomass Burning
NO <sub>x</sub>	50%	200%	100%
VOC	150%	200%	300%

**Table 4.** Statistics of surface temperature, relative humidity, and wind. Corr – Correlation;; RMSE – Root Mean Square Error; MAE – Mean Absolute Error; MB – Mean Bias; O – Observation; M - Model; O\_M – Observed Mean; M\_M – Model Mean; SD – Standard Deviation; Units for RMSE/MAE/MB/O\_M/M\_M/O\_SD/M\_SD: °C for temperature, percentage for relative humidity, and m s<sup>-1</sup> for wind.

Variable	Corr	RMSE	MAE	MB	O_M	M_M	O_SD	M_SD
Temperature	0.74	7.0	2.8	0.6	22.2	22.8	9.5	8.7
Relative Humidity	0.76	12.1	9.5	-1.1	67.8	66.6	14.3	18.6
U Wind	0.58	1.3	0.7	0.1	0.1	0.2	1.2	1.4
V Wind	0.49	1.6	0.7	0.3	0.2	0.5	1.6	1.2

**Table 5.** NO<sub>x</sub> emissions before and after carrying out the inversion using OMI/OMPS for different countries in May-June 2016.

<b>Countries</b>	<b>The a priori (Gg/day)</b>	<b>The a posteriori (Gg/day)</b>	<b>Changes in magnitudes</b>	<b>Changes in errors</b>
China	87.94±44.09 <sup>1</sup>	68.00±15.94 <sup>2</sup>	-23%	-63%
North China Plain	27.96±13.49	19.05±2.50	-32%	-81%
Pearl River Delta	4.23±1.78	2.70±0.32	-36%	-84%
Yangtze River Delta	9.84±4.68	5.77±0.51	-41%	-89%
Thailand	4.38±3.24	4.20±2.28	-4%	-29%
Japan	3.53±1.71	3.96±1.04	+12%	-39%
Malaysia	2.89±2.77	2.25±1.34	-22%	-49%
Vietnam	2.87±2.04	2.79±1.57	-3%	-23%
South Korea	2.71±1.34	2.95±0.58	+9%	-56%
Bangladesh	1.72±1.06	2.10±0.87	+22%	-18%
Philippines	1.30±1.10	1.54±0.98	+18%	-11%
Taiwan	1.26±0.57	0.97±0.33	-23%	-42%
Cambodia	0.54±0.50	0.57±0.45	+5%	-11%
Mongolia	0.19±0.13	0.28±0.12	+44%	-8%

- 925 1- The errors in the a priori are estimated from equation 6.  
 2- The errors in the a posteriori are calculated by equation 4.

**Table 6.** MDA8 surface ozone levels before and after carrying out the inversion for different regions in May-June 2016.

<b>Regions</b>	<b>The a priori (ppbv)</b>	<b>The a posteriori (ppbv)</b>	<b>Changes in magnitudes</b>
China	56.10±16.34	56.72±16.71	+1.1%
North China Plain	81.15±9.57	85.71±10.39	+5.6%
Pearl River Delta	65.94±9.39	62.37±8.93	-5.4%
Yangtze River Delta	76.79±5.90	82.04±5.21	+6.8%
Thailand	50.86±8.84	48.85±7.94	-3.9%
Japan	64.29±7.98	65.52±7.78	+1.9%
Malaysia	46.87±21.87	44.22±12.90	-5.6%
Vietnam	49.90±9.20	48.88±8.65	-2.0%
South Korea	84.23±3.57	84.90±3.69	+0.8%
Bangladesh	65.79±12.08	65.21±12.20	-0.9%
Philippines	27.92±9.11	28.69±7.92	+2.8%
Taiwan	61.55±10.88	54.38±8.00	-11.6%
Cambodia	39.87±3.62	40.20±3.46	+0.8%
Mongolia	40.11±2.52	40.16±2.40	+0.1%

930

935 Figures:

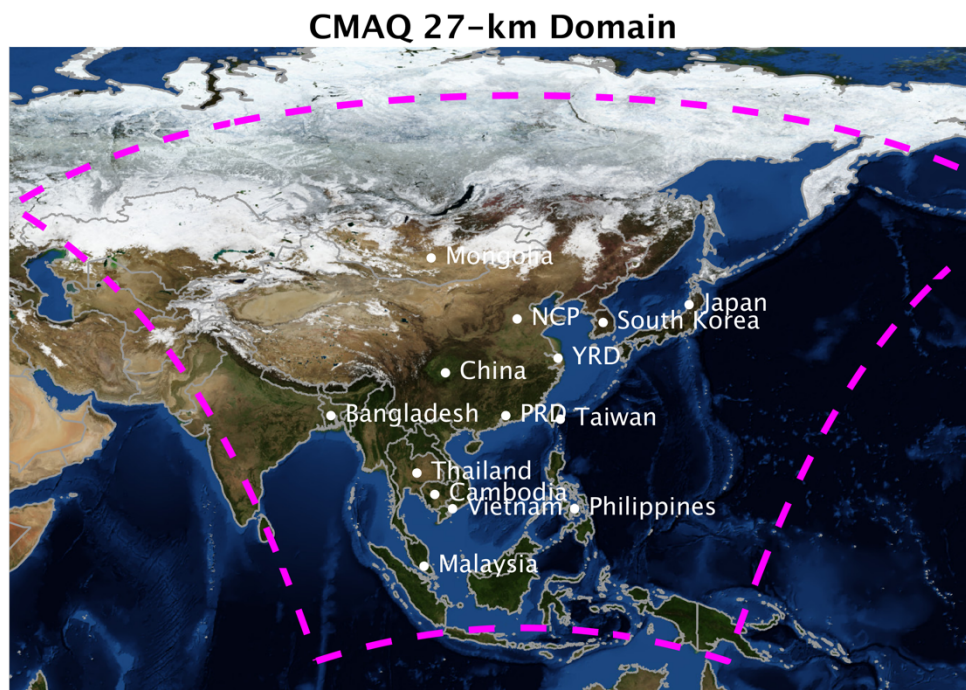


**Figure 1.** The CMAQ 27-km domain covering the major proportion of Asia. The background picture is retrieved from publicly available NASA's blue marble (© NASA).



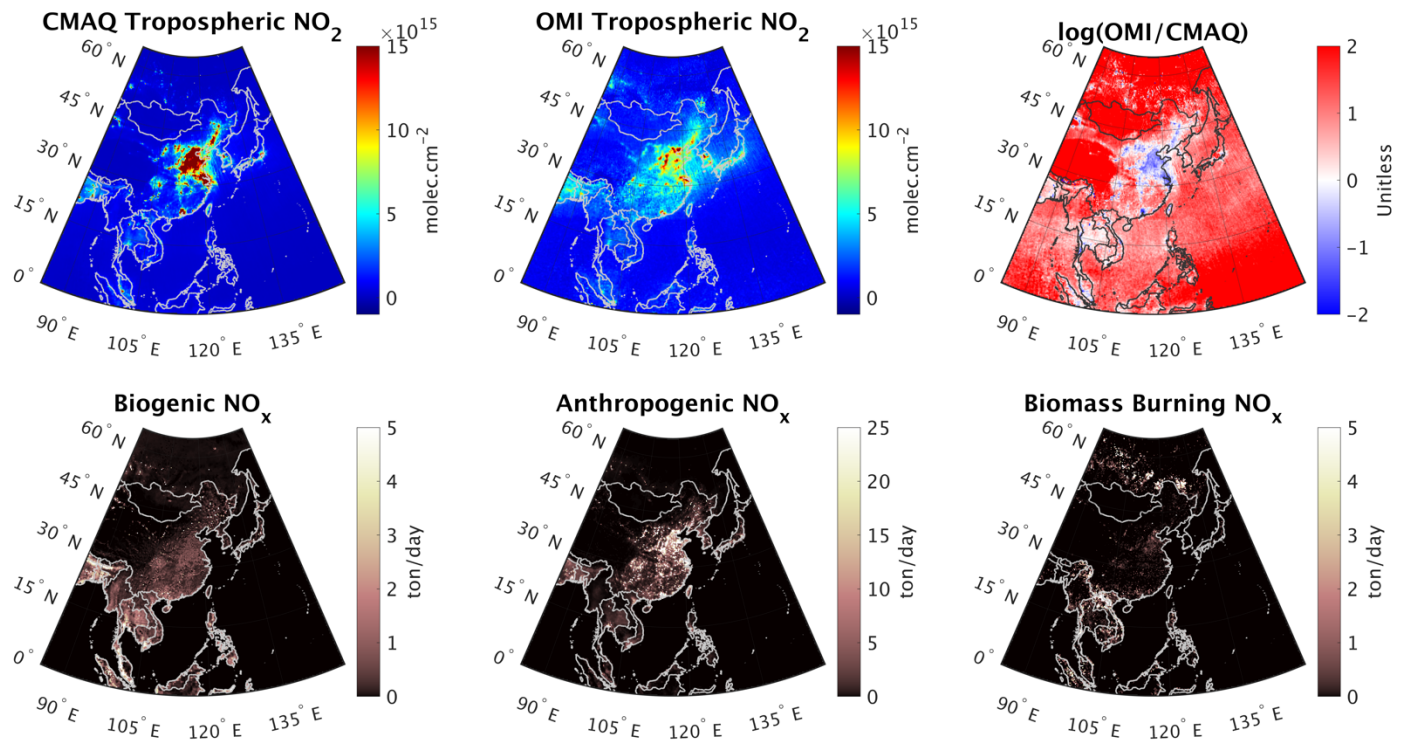
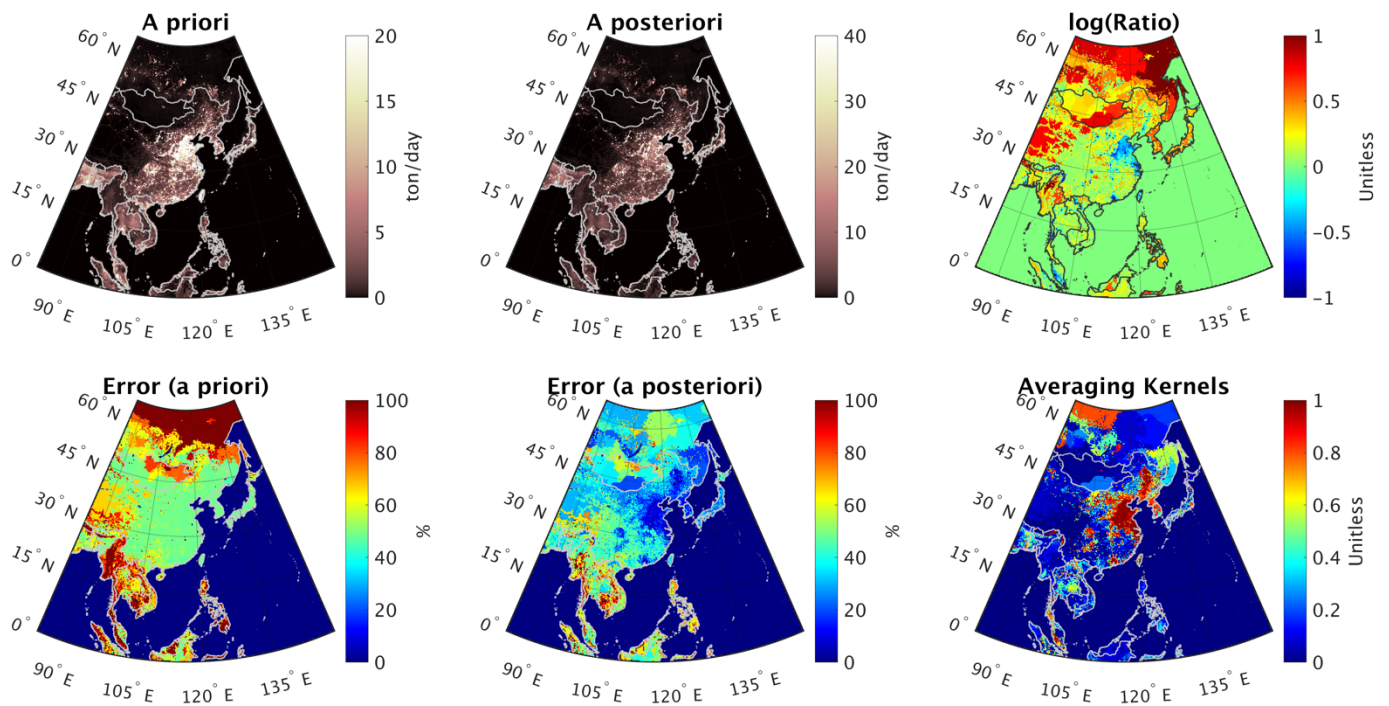


**Figure 2.** (first row), tropospheric NO<sub>2</sub> columns from the WRF-CMAQ model, OMI (using adjusted AMFs based on the shape factors derived from the model and bias corrected following Choi et al. [2019]), and the natural logarithmic ratio of OMI/CMAQ during May-June 2016 at ~1330 LST. (second row) The major sources of NO<sub>x</sub> emissions in the region including biogenic (soil) emissions simulated by MEGAN, anthropogenic emissions estimated by MIX Asia (2010), and biomass burning emissions made by FINN. The emissions are the daily-mean values based on the emissions in May-June.



95( **Figure 3.** (first row), total NO<sub>x</sub> emissions (i.e., the a priori), constrained by the satellite observations (i.e., the a posteriori) in May-June 2016, and the natural logarithmic ratio of the a posteriori to the a priori. (second row) the errors in the a priori based on Table 3, the errors in the top-down estimation, and the averaging kernels (AKs) obtained from the estimation.

955

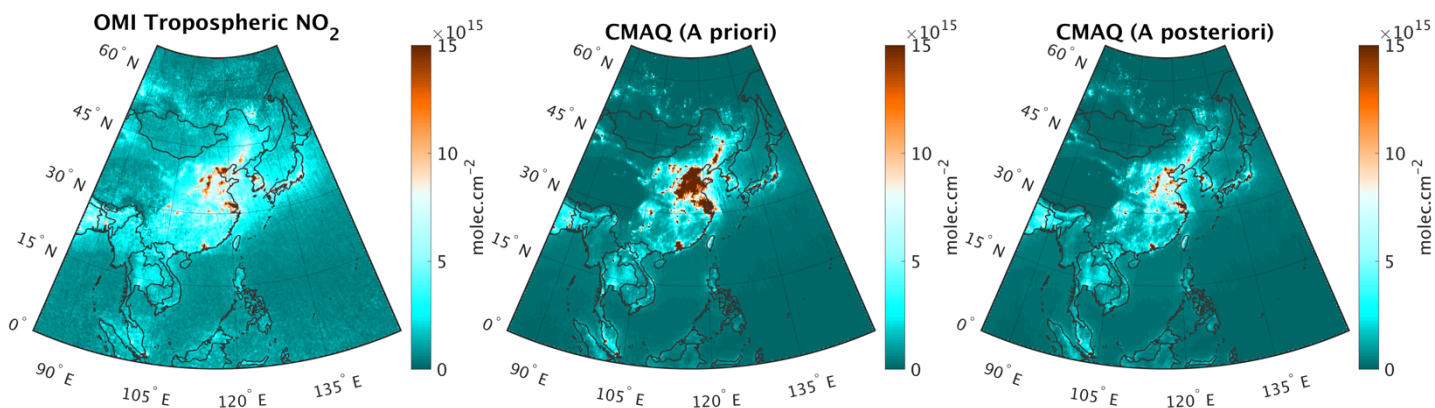


**Figure 4.** (from left to right), tropospheric NO<sub>2</sub> columns from OMI, WRF-CMAQ simulated with the prior emissions, and the same model but with the top-down emissions constrained by 960 OMI/OMPS in May-June 2016.

965

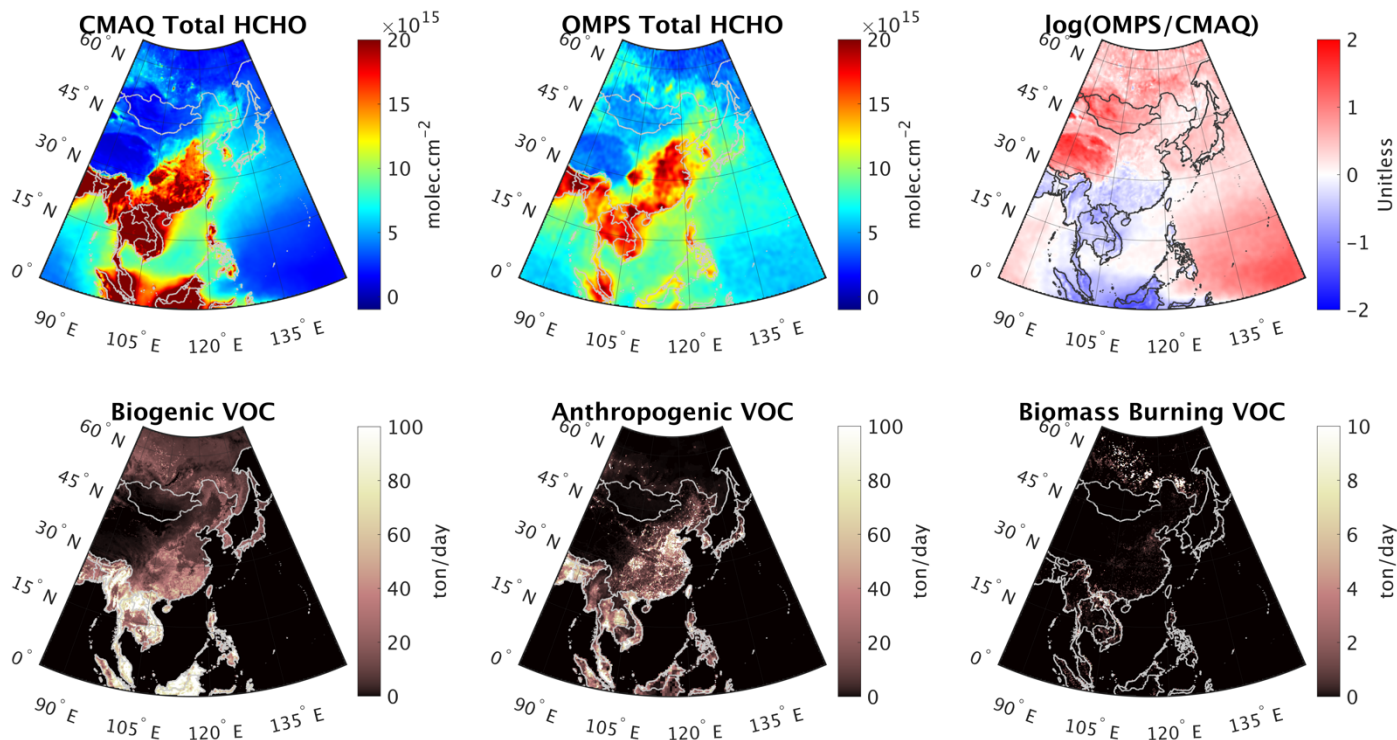


**Figure 5.** (first row), HCHO total columns from the WRF-CMAQ model, OMPS (using adjusted AMFs based on the shape factors derived from the model and bias corrected following the method proposed in Zhu et al. [2020]), and the natural logarithmic ratio of OMPS/CMAQ during May-June 2016 at  $\sim 1330$  LST. (second row) The major sources of VOC emissions in the area including biogenic emissions simulated by MEGAN, anthropogenic emissions estimated by MIX Asia (2010), and biomass burning emissions made by FINN. The emissions are the daily-mean values based on the emissions in May-June. The VOC emissions only add up those compounds that are included in the CB05 mechanism.

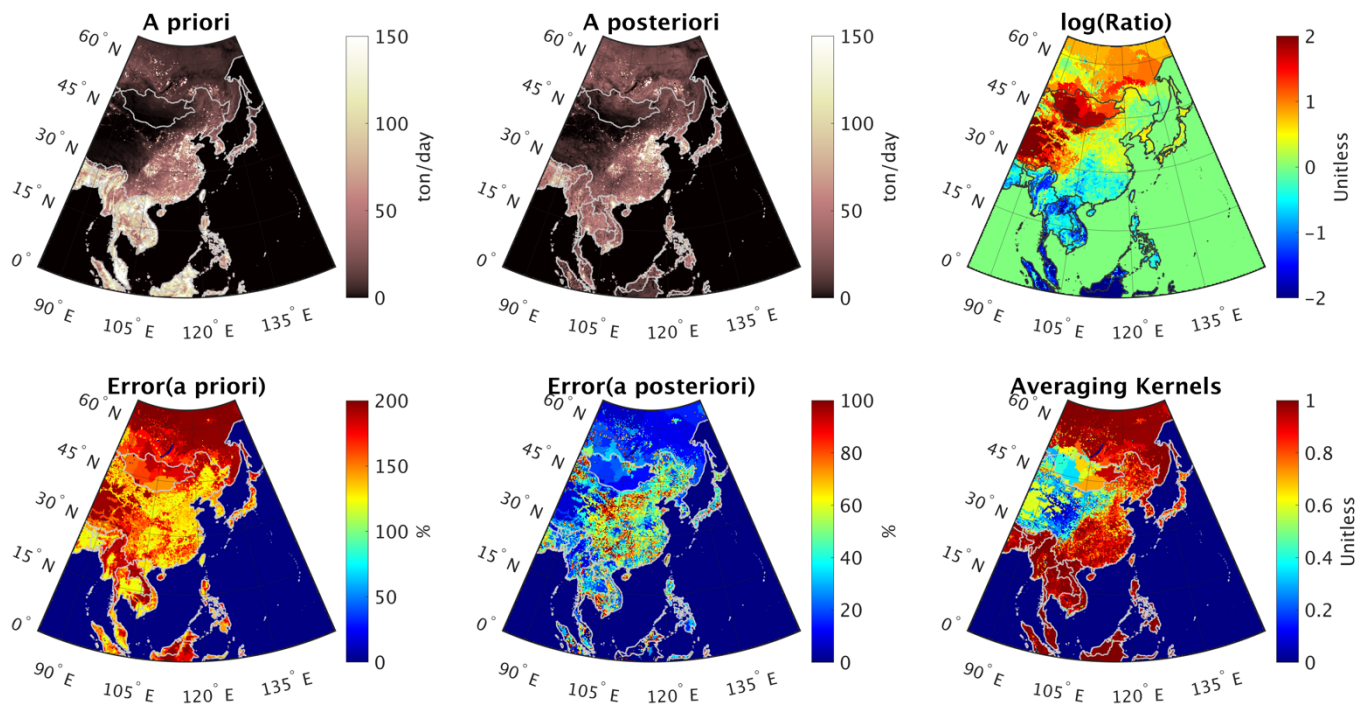


**Figure 6.** (first row), total VOC emissions (i.e., the a priori), constrained by the satellite observations (i.e., the a posteriori) in May-June 2016, and the natural logarithmic ratio of the a posteriori to the a priori. (second row) the errors in the a priori based on Table 3, the errors in the top-down estimation, and the averaging kernels (AKs) obtained from the estimation.

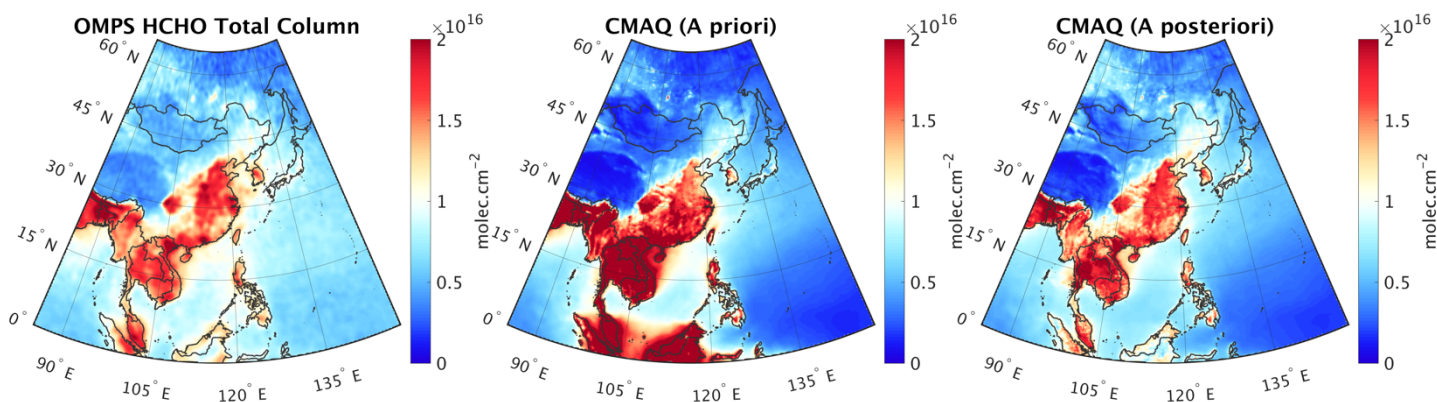


**Figure 7.** (from left to right), HCHO total columns from OMPS, the WRF-CMAQ simulated with the prior emissions, and the same model but with the top-down emissions constrained by the satellites in May-June 2016.

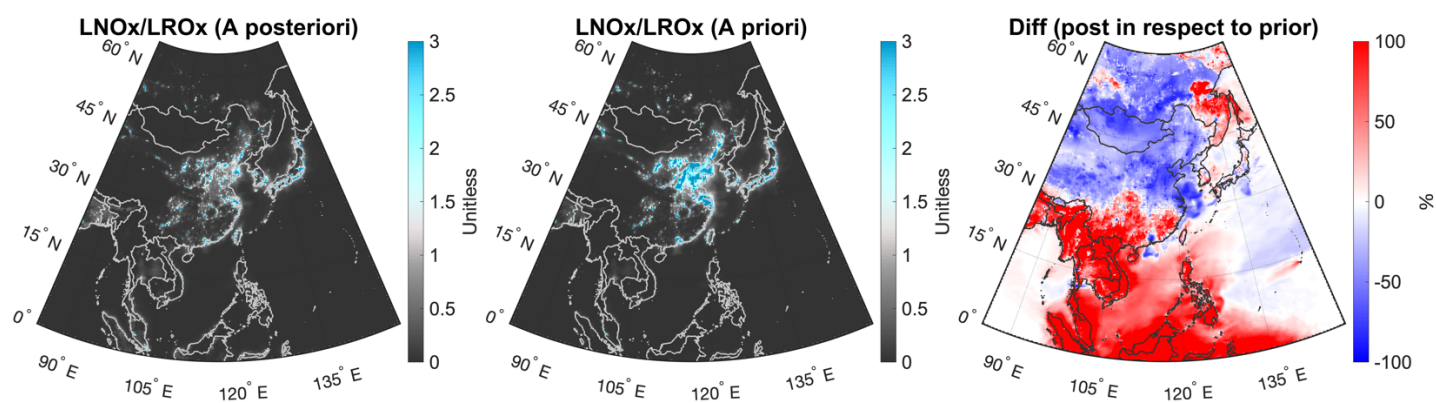


**Figure 8.** (from left to right), ratio of LNO<sub>x</sub>/LRO<sub>x</sub> simulated by the posterior emissions, the prior, and their relative differences at 1200-1800 CST, averaged over May-June 2016.

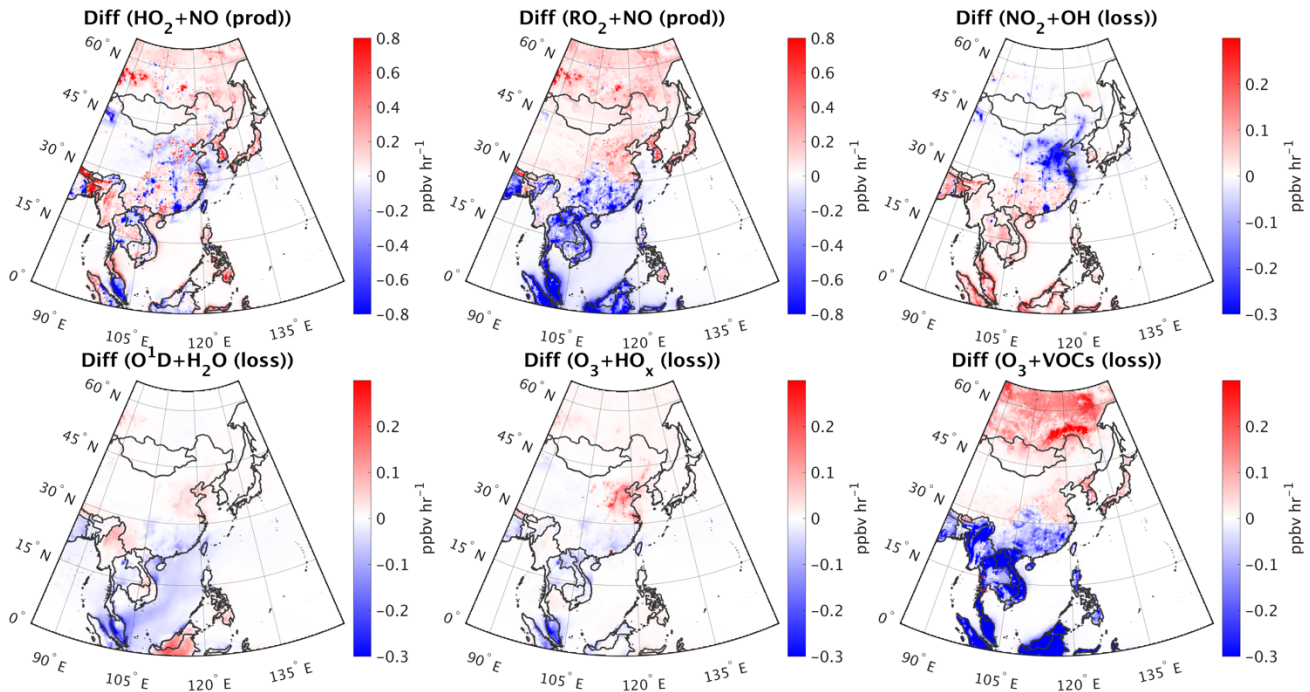


**Figure 9.** Differences between the simulations with the updated emissions and the default ones of six major pathways of ozone production/loss. The time period is May-June 2016, 1200-1800 CST.

995

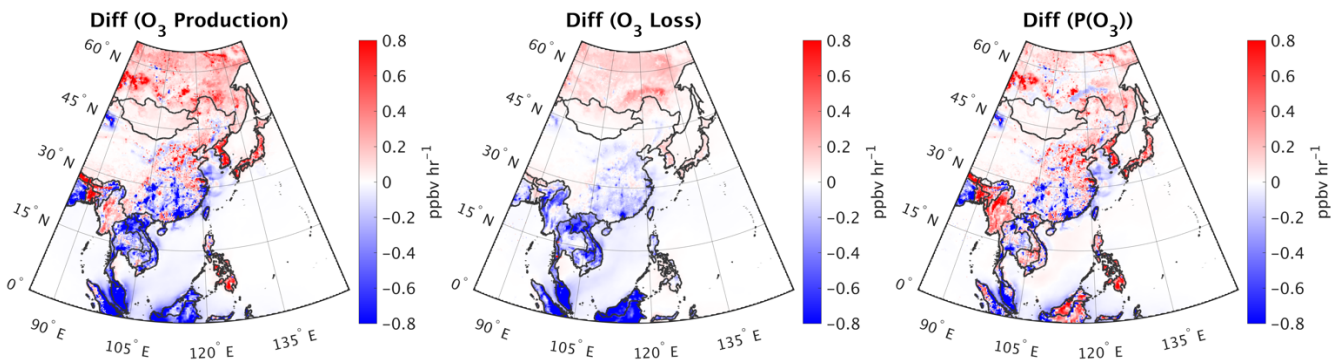


**Figure 10.** Changes in the major chemical pathways of ozone production/loss, and the net of ozone production  $P(O_3)$  after updating the emissions. The time period is May-June 2016, 1200-1800 CST.

1000

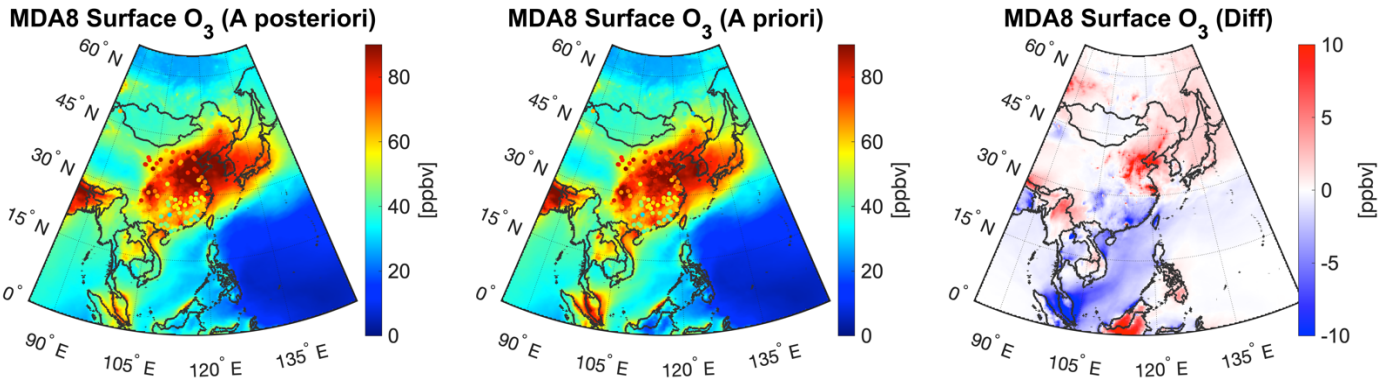


**Figure 11.** Simulated MDA8 surface ozone using the updated emissions constrained by OMI and OMPS observations (left), the default ones (middle), and their difference (right) in May-June 2016. We overplot surface MDA8 ozone values (circles) from the Chinese air quality monitoring network (<https://quotsoft.net/air/>).